ACS Catalysis

pubs.acs.org/acscatalysis Research Article

Computational Characterization of the Inhibition Mechanism of Xanthine Oxidoreductase by Topiroxostat

Yazdan Maghsoud, Chao Dong, and G. Andrés Cisneros*

Cite This: *ACS Catal.* 2023, 13, 6023−6043 Read Online

ACCESS | Metrics & More | Article Recommendations | Supporting Information

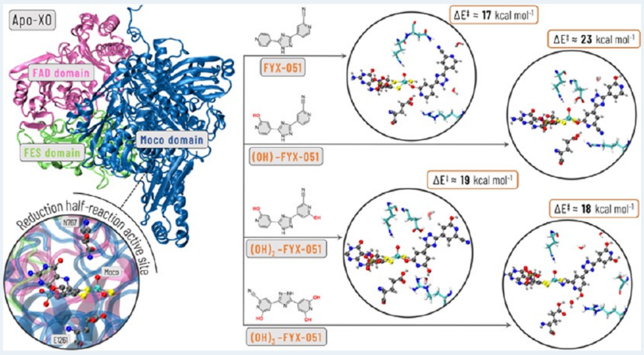

ABSTRACT: Xanthine oxidase (XO) is a member of the molybdopterin-containing enzyme family. It interconverts xanthine to uric acid as the last step of purine catabolism in the human body. The high uric acid concentration in the blood directly leads to human diseases like gout and hyperuricemia. Therefore, drugs that inhibit the biosynthesis of uric acid by human XO have been clinically used for many years to decrease the concentration of uric acid in the blood. In this study, the inhibition mechanism of XO and a new promising drug, topiroxostat (code: FYX-051), is investigated by employing molecular dynamics (MD) and quantum mechanics/molecular mechanics (QM/MM) calculations. This drug has been reported to act as both a noncovalent and covalent inhibitor and undergoes a stepwise inhibition by all its hydroxylated metabolites, which include 2-hydroxy-FYX-051, dihydroxy-FYX-051, and trihydroxy-FYX-051. However, the detailed mechanism of inhibition of each metabolite remains elusive and can be useful for designing more effective drugs with similar inhibition functions. Hence, herein we present the computational investigation of the structural and dynamical effects of FYX-051 and the calculated reaction mechanism for all of the oxidation steps catalyzed by the molybdopterin center in the active site. Calculated results for the proposed reaction mechanisms for each metabolite's inhibition reaction in the enzyme's active site, binding affinities, and the noncovalent interactions with the surrounding amino acid residues are consistent with previously reported experimental findings. Analysis of the noncovalent interactions via energy decomposition analysis (EDA) and noncovalent interaction (NCI) techniques suggests that residues L648, K771, E802, R839, L873, R880, R912, F914, F1009, L1014, and A1079 can be used as key interacting residues for further hybrid-type inhibitor development.

KEYWORDS: *xanthine oxidoreductase, topiroxostat, FYX-051, molecular dynamics, quantum mechanics/molecular mechanics, inhibition mechanism*

1. INTRODUCTION

Molybdenum hydroxylases are a family of enzymes that catalyze the hydroxylation of various heterocyclic substrates like purines, pyrimidines, and aldehydes, which can be found in nearly all eukaryotic and prokaryotic organisms.[1−10] Mammalian xanthine oxidoreductase (XOR) is a member of this family and catalyzes the sequential hydroxylation of hypoxanthine to xanthine and xanthine uric acid during the last two steps of the purine degradation pathway.[11,12] The molecular mass of this homodimeric enzyme is around 300 kDa. As shown in Figure 1A, each subunit contains one pterin-based molybdenum cofactor (Moco), one flavin adenine dinucleotide (FAD), and two iron−sulfur clusters (FES).[13−15] The active site of XOR includes the Moco center, where the hydroxylation of the natural substrates, i.e., xanthine or hypoxanthine, takes place and results in the reduction of the molybdenum cation from Mo^{6+} to Mo^{4+} (see Scheme 1A).[16,17]

Contrary to most oxidases that use molecular oxygen for the oxidation reaction, the oxygen source for the XOR is a water molecule.[15,16] After fulfilling the hydroxylation at the Moco active site, the electron transfer occurs via the iron−sulfur clusters to the FAD, where the oxidization of the enzyme is completed by the physiological electron acceptor, NAD^+ or O_2.[11] Coded by the same gene, the mammalian XOR exists in two alternative forms, XO (xanthine oxidase) and XDH (xanthine dehydrogenase).[11,12] In contrast with XDH, which can utilize either the NAD^+ or O_2 as the oxidizing substrate, XO—the oxidized form of the XDH by oxidation of sulfhydryl residues or by limited proteolysis—can exclusively react with molecular oxygen (see Figure 1B).[18]

Received: March 18, 2023
Revised: April 3, 2023
Published: April 18, 2023

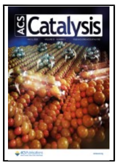

https://doi.org/10.1021/acscatal.3c01245
ACS Catal. 2023, 13, 6023−6043

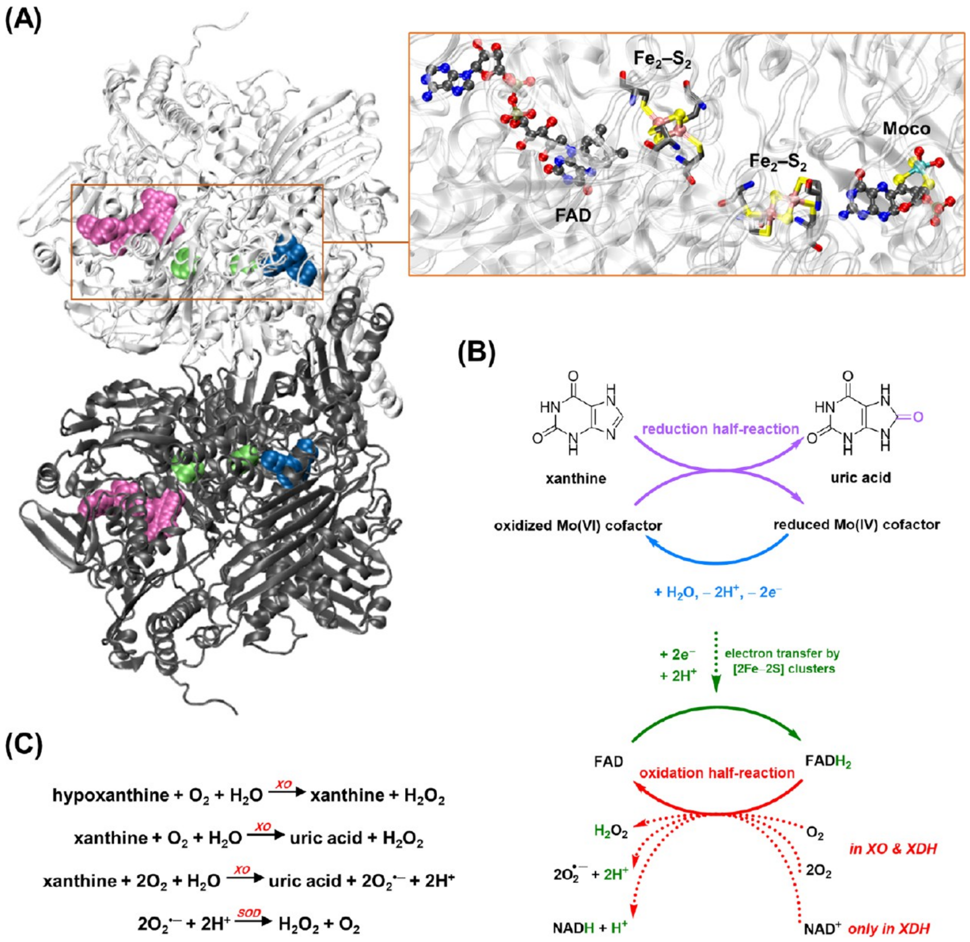

Figure 1. (A) Crystal structure of the bovine xanthine oxidoreductase dimer (white and gray) along with the molybdenum cofactor (blue), iron–sulfur clusters (green), and the flavin adenine dinucleotide (mauve) in each subunit (PDB ID: 1JRO).[44] The magnified close-up of the XOR's active region in the reductive–oxidative half-reactions shows Moco (right), Fe_2–S_2 clusters, each bridged between four cysteine residues (middle), and the FAD (left). Hydrogen atoms are not presented for more clarity, and four cysteine residues bound to the irons of each Fe_2–S_2 cluster are shown in the sticks. (B) The scheme of the reductive–oxidative half-reactions occurring in XOR and XDH during the hydroxylation of xanthine to uric acid. The scheme is adapted from Metz and Thiel.[78] (C) The irreversible production of uric acid and hydrogen peroxide by human XO. The superoxide dismutase enzyme (SOD) catalyzes the transformation of superoxide anion radicals into molecular oxygen and hydrogen peroxide.

Production of uric acid and hydrogen peroxide by XOR in humans is the final, irreversible step without further metabolism (see Figure 1C). The produced uric acid is excreted mainly by the kidneys and partly by the intestinal tract.[19,20] Clinical studies showed that high blood concentrations of uric acid lead to gout and hyperuricemia, associated with other medical conditions such as diabetes and the formation of kidney stones.[21−27] To cure the diseases above, uric acid excretion has to be increased or its production needs to be decreased.[28,29] Several investigations demonstrated that the later treatment, by which inhibitors hinder the function of XOR, not only cures gout and hyperuricemia but may also help treat other diseases.[30,31]

Allopurinol, a hypoxanthine analog, was the first drug that emerged as a "gold-standard" inhibitor of xanthine oxidase in the early 1960s.[32,33] Later, it was realized that the xanthine oxidase hydroxylates allopurinol to give oxipurinol, the active form that inhibits XOR (see Scheme 1B).[34] With its excellent pharmacokinetic properties, oxipurinol has been widely prescribed for decades. However, because of the short dissociation half-life ($t_{1/2} \approx 300$ min),[34] high doses of this drug are usually administered, which may cause severe side effects such as Stevens–Johnson syndrome (SJS), renal failure, and fulminant hepatitis.[35−37] Several potent and longer-lasting inhibitors with structural or/and mechanistic inhibition have been introduced to cope with these drawbacks.[38−55] Some of these candidates with promising inhibitory effects, such as TEI-6720 (febuxostat),[45,56−58] Y-700 (piraxostat),[48,59,60] BOF-4272,[42,55,61] and FYX-051 (topiroxostat),[46,47,62−65] have been studied more extensively (chemical structures are given in Scheme 1B,C).

Among the mentioned candidates, febuxostat obtained approval from the U.S. FDA, the European medicine agency, and the Japanese authorities to treat gout. Furthermore, in 2013, topiroxostat was accepted in Japan based on its better therapeutic effects on gout and hyperuricemia. In addition, long inhibition half-life ($t_{1/2} \approx 20.4$ h) after administration,[46,47] good oral bioavailability, and other pharmacological features made topiroxostat a new-generation inhibitor.[66] Despite the advantages of topiroxostat, searching for new drugs continues[67−74] due to the increasing number of reported cases suffering from gout.[75−77]

Unlike the mechanism-based inhibitors, which bind covalently to the molybdenum cofactor,[32−34,79] or the structure-based inhibitors having noncovalent interactions—such as hydrogen bonds, salt bridges, hydrophobic interactions,

Scheme 1. (A) Suggested Mechanism for XO's Catalytic Hydroxylation of Xanthine; (B, C) Some Known XOR Inhibitors: Allopurinol and Oxipurinol Are Mechanism-Based Inhibitors; BOF-4272, TEI-6720, and Y-700 Are Nonpurine Structure-Based Inhibitors, While FYX-051 and Its Hydroxylated Derivatives Are Hybrid-Type Inhibitors; (D) Left: Coordination Mode in Moco−FYX-051, Showing a Covalent Linkage between the Bridging Oxygen of Moco and the C2 Atom of the Substrate (PDB ID: 1V97).[46] Middle: Coordination Mode in Moco−trihydroxy-FYX-051, Showing a Direct Bond between the Nitrile's Nitrogen Atom and the Molybdenum of Atom Moco (PDB ID: 3AM9).[47] Right: Coordination Mode in Moco−oxipurinol, in which the Water-Exchangeable Hydroxide (OH^-) Is Replaced by N2 Nitrogen of Oxipurinol (PDB IDs: 1JRP and 3BDJ).[44,80]

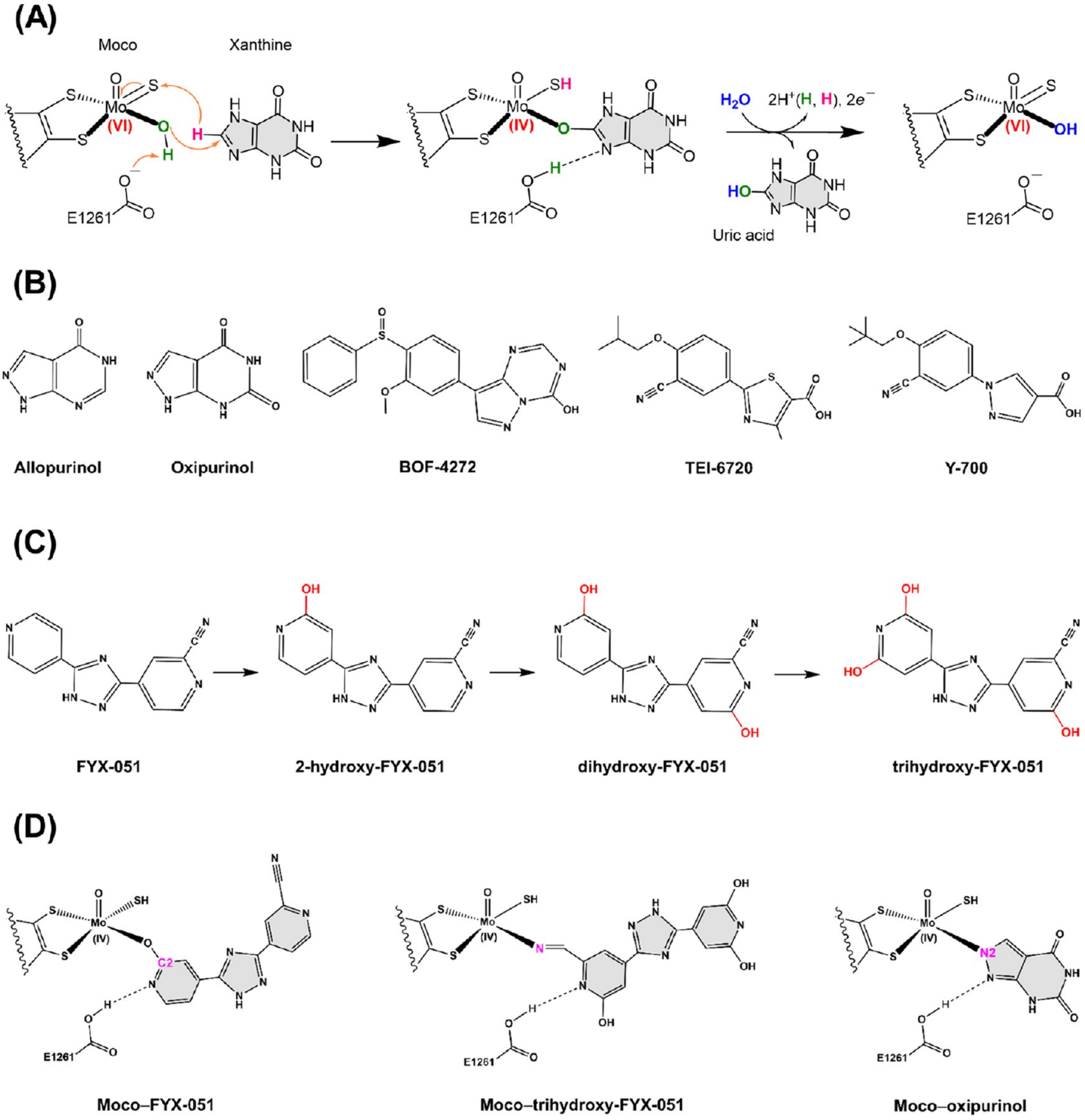

$\pi-\pi$ interactions, and van der Waals interactions—with the protein matrix,[42,45,60,74] topiroxostat is a hybrid-type inhibitor showing both inhibitory traits. In the remainder of this work, we will refer to topiroxostat by its code, FYX-051. Nishino and co-workers[46] showed that FYX-051 forms a covalent bond with the Moco (Scheme 1D, left), undergoes hydroxylation by the enzyme, and fills up the active site channel by interacting with the surrounding amino acids. This hybrid performance efficiently prevents substrate binding and inhibits XOR's activity for up to 20.4 h.

Another effort by Nishino and co-workers[47] indicated that FYX-051 goes through sequential XOR-mediated hydroxylation during prolonged incubation for up to 72 h. LC/MS analysis coupled with NMR spectroscopy showed that FYX-

051 converts to 2-hydroxy-FYX-051, dihydroxy-FYX-051, and trihydroxy-FYX-051 (structures are shown in Scheme 1C). Their crystallographic analysis revealed the new crystal structure of Moco−trihydroxy-FYX-051, which is entirely different from Moco−FYX-051. Similar to the Moco−oxipurinol (Scheme 1D, right),[44,80] the substrate in this structure is directly coordinated to the reduced molybdenum ion via the nitrogen atom (see Scheme 1D, middle). Steady-state kinetic studies provided the K_i values for the noncovalent inhibition by the FYX-051 and its first hydroxylated metabolite, 2-hydroxy-FYX-051 (5.7×10^{-9} and 1.5×10^{-6} M, respectively). However, the kinetics of the chemistry step, i.e., the reduction half-reaction, as well as probable inhibition effects by the other metabolites, remains to be investigated.

So far, several experimental[81−89] and computational[78,90−98] studies have been reported on the hydroxylation reaction of hypoxanthine/xanthine and other purine- or nonpurine-based inhibitors by the XOR. Considering all of the mentioned features of FYX-051 and the possible inhibitory effects of its hydroxylated metabolites, a comprehensive atomistic investigation of the kinetics of the inhibition reaction can aid in further developing more efficient hybrid-type XOR inhibitors. In this study, we employed classical molecular dynamics (MD) and quantum mechanics/molecular mechanics (QM/MM) to study the thermodynamics and kinetics of the hydroxylation reaction between the Moco center and FYX-051, including all its possible metabolites. The remainder of the paper is as follows; in the next section, we describe the approach for the MD and QM/MM simulations, including the relative binding affinity determination for all metabolites, reaction path optimization, and structural, dynamical, and kinetic analyses for all of the ligands. Subsequently, the results for each metabolite and their implication with respect to each other are presented and discussed, followed by concluding remarks.

2. COMPUTATIONAL METHODS

2.1. Molecular Dynamics (MD) Simulations.

2.1.1. Structural Model. The crystal structures of bovine milk xanthine dehydrogenase bound to FYX-051 (PDB ID: 1V97)[46] and trihydroxy-FYX-051 (PDB ID: 3AM9)[47] were used as the initial models. The starting structures for XO−2-hydroxy-FYX-051 and XO−dihydroxy-FYX-051 were constructed from 1V97. The sequence alignment via BLAST[99,100] between the human XOR[89,101] and the bovine form shows a similarity of ≈90%. The missing regions in 1V97 include residues 1, 2, 166−191, and 531−536, while in 3AM9, residues 1321−1325 were also missing. These gaps account for less than 3% of the entire amino acid sequences, located in flexible loops of the protein's surface and far from the redox reaction region, i.e., Moco, iron−sulfur clusters, and the FAD (see Figure S1A,B). MODELLER 10.1[102,103] was used to perform comparative modeling of XOR's three-dimensional structure and incorporate the missing residues into the PDB structures. CASP[104] and CAMEO[105] assessment techniques were used to evaluate the accuracy of the computed models by MODELLER, and the best-fitted PDB structures were employed for further MD simulations (see Figure S1C,D).

2.1.2. MD Setup. In addition to the studied substrates, i.e., FYX-051, 2-hydroxy-FYX-051, dihydroxy-FYX-051, and trihydroxy-FYX-051, molybdenum cofactor (Moco), flavin adenine dinucleotide (FAD), and iron−sulfur cluster (FES) needed to be parameterized (see Figure S2). The AMBER force field parameters for the Moco were obtained from the publication by Ramos and co-workers.[106] Parameters for the iron−sulfur cluster were calculated via the MCPB.py module (version 3.0) of AMBER18,[107] while the remaining missing parameters were obtained from Ramos and co-workers.[108] All of the substrates and the FAD were initially parameterized by the R.E.D. Server,[109−111] whereas the missing bonded parameters were added by ANTECHAMBER.[112,113] The protonation of all of the amino acid residues was assessed via the PROPKA software.[114,115] In addition, the protonation state of E1261 and E802 in the active site is a key factor in the system setup. Experimental[46,88,89,116,117] and computational[118] results show that E1261 is deprotonated before the redox reaction. E802 is commonly assumed to be in its protonated form when the natural substrate or oxipurinol is in the binding pocket, participating in hydrogen-bonding interaction, albeit deprotonation is facile.[44,48,80,89,119]

The LEaP module[120] in AMBER18[121] was used to add the hydrogen atoms, neutralize the system with the corresponding number of required counterions, and solvate the structure in a cubic box filled with TIP3P[122] water, extending at least 12 Å from the protein surface. The ff14SB[123] and GAFF[112] force fields were used to describe the system. The MD simulations were done via AMBER18 pmemd.cuda.[121] Seven minimization steps were performed with decreasing restraint (10.0−0.0 kcal $\mathrm{mol^{-1}}$ $\mathrm{Å^{-2}}$) on the solute's heavy atoms. In each stage, the system was minimized within 5000 cycles of minimization via the steepest descent algorithm, continuing with 5000 cycles via the conjugated gradient algorithm. In the next step, each system was heated to 300 K using Langevin dynamics[124−126] with a collision frequency of 2 $\mathrm{ps^{-1}}$ followed by 7 ns of NVT equilibration with decreasing restraint (10.0−0.0 kcal $\mathrm{mol^{-1}}$ $\mathrm{Å^{-2}}$) on the protein's heavy atoms. Lastly, the production calculations for each system were accomplished in 500 ns of NPT ensemble[124,126] without restraint in triplicate—a total of 1.5 μs for each system. All bonds involving hydrogen atoms were treated using SHAKE,[127] and long-range Coulomb interactions[128] were handled with the smooth particle mesh Ewald method[129] using a 10 Å cutoff for nonbonded interactions.

2.1.3. Structural Analysis. The CPPTRAJ[130] module in AMBER18 was used to analyze production dynamics, i.e., RMSD, RMSF, and correlation matrices. Normal mode analysis was performed using the ProDy code.[131] In addition, Python libraries NumPy,[132,133] Matplotlib,[134] Pandas,[135] statsmodels[136] module, and Gnuplot[137] command-line were also employed for further data processing and graphing. All of the studied systems were stable without significant fluctuations during the production MD simulations (Figures S3−S17), which were used for further clustering analysis. To perform the clustering analysis, 150,000 trajectories from 300 to 500 ns of three replicates of each system were used for a multidimensional analysis via the *k*-means algorithm[138] implemented in AMBER's CPPTRAJ. Each dimension of this analysis on the reaction's active site corresponds to important distances and angles between the Moco, substrate, and E1261 (except in trihydroxy-FYX-051). Ten clusters containing three representatives were initially obtained to find the closest representatives to the centroids of each cluster in the studied systems. In the next step, three clusters (nine representatives) for XO−FYX-051 and XO−dihydroxy-FYX-051 and two clusters (six representatives) for XO−2-hydroxy-FYX-051 and XO−trihydroxy-FYX-051 with the highest population abundance and the best orientations of the active site's residues involved in the inhibition reaction were selected for further QM/MM optimizations (Figures S18−S21).

2.2. MM/GBSA Analysis. Binding affinities between the ligand (FYX-051 metabolites) and the receptor (XO) were studied by calculating the total binding energies via molecular mechanics/generalized Born surface area (MM/GBSA).[139−141] MM/GBSA computations were performed based on the "single-trajectory" protocol, that is, one trajectory of the system,[142] in which the last 10,000 frames of all three replicates of each structure were used for the calculations (30,000 frames in total). Relative binding enthalpy computations were performed via the MMPBSA.py internal module of AmberTools, employing the default values for the offset and surface tension to correct the nonpolar contribution to the solvation free energy, and salt concentration was set to 150 mM.[143] Entropy contributions were neglected, given the focus of the calculations on relative binding affinities only, the similarity of the ligands, and to avoid potential convergence issues.[144−150]

2.3. QM/MM Calculations. All of the QM/MM calculations of the studied systems were carried out via LICHEM,[151,152] interfacing between Gaussian16[153] and TINKER.[154] The QM region and the MM environment were described with the ωB97X-D/def2-SVP[155,156] level of theory and the AMBER ff14SB force field, respectively. The basis set for the QM atoms was obtained from the basis set exchange library.[157] The QM/MM long-range electrostatic correction (QM/MM-LREC) method[158] with a 25 Å cutoff, along with the particle mesh Ewald[128] (PME) method, was employed for the QM subsystem and the MM calculations, respectively. The QM subsystem in each structure includes Moco, the substrate of interest, E1261, E802, and Q767 (a total of 87−92 atoms, depending on the substrate), while the remaining residues and all solvent molecules were described with ff14SB potential. In the case of the complexation between Moco and the first three metabolites, in which the oxidation state of the Mo atom is (VI), the singlet spin multiplicity is preferred, as reported previously.[95,106] Various multiplicities were tested regarding the last metabolite coordinating with the reduced Moco during the enzymatic turnover.[159] However, in agreement with Cerqueira and co-workers,[95] the most stable state corresponds to a singlet multiplicity. To treat the covalent boundaries of the QM subsystem's amino acids, the pseudobond approach[160] was applied. The iterative QM/MM optimization protocol implemented in LICHEM[151,152] was carried out for the optimization, in which all atoms in the MM subsystem within a radius of 27 Å from the Mo center were optimized and the rest were kept frozen.

After optimizing each system's selected representatives, the one with the lowest QM/MM optimization energy was considered the most stable reactant, and the product was designed based on that structure. The designed products were then used for further QM/MM calculations at the same level of theory. Based on the optimized reactant and the product structures of each system, the quadratic string method (QSM) combined with the restrained-MM procedure implemented in LICHEM[152] was used to obtain and compare the potential energy surface of the reaction path. The initial restraint on the MM environment was set to 50 kcal mol^{-1} Å^{-2} and removed stepwise. The reaction path was considered a chain of 14 beads between the reactant (bead 0) and the product (bead 15), resulting in 16 total beads.

2.4. NCI and ELF Analyses. The noncovalent interactions (NCIs) between the ligand (FYX-051 and its metabolites) and the surrounding amino acids in the binding pocket were analyzed via the promolecular density method[161] embedded in the Multiwfn V. 3.8 program.[162] This analysis qualitatively illustrates the chemical bonding and weak noncovalent interactions based on the relationship between the electronic density and the reduced density gradient in regions of low electron density. The strength and characteristics of the NCI surfaces are color-coded in the RGB scale, in which green and blue surfaces represent strong and weak interactions like hydrogen bonds and van der Waals, whereas the red surfaces show repulsive interactions. These surfaces were visualized with an isovalue of 0.4 a.u. and a color scale of −0.05 a.u. < sign(λ_2)ρ < 0.05 a.u. All of the wave functions for the electron localization function (ELF) analysis[163] were obtained from the structures of the reactant, product, and the approximate TS optimized by the QM/MM calculations. The ELF calculations were performed via the basin analysis[164,165] embedded in the Multiwfn V. 3.8 program.[162] A cubic grid of 200 a.u. with an isovalue of 0.8 a.u. and medium quality grid with a spacing of 0.10 Bohr were selected for the basin illustration. Visual molecular dynamics (VMD)[166] was used for rendering the images.

2.5. Energy Decomposition Analysis (EDA). Energy decomposition analysis is an approach to investigate the nature of the intermolecular interactions between the protein and any fragment(s) of interest, which is based on the calculation of the averaged energies of the nonbonded intermolecular interactions as a function of a particular reference residue(s). EDA has been used to analyze the MD and QM/MM calculations of several protein systems,[167−173] which gives a qualitative assessment of the catalytic role of amino acid residues surrounding the active site. In this study, EDA was employed on both the MD simulations and QM/MM optimizations to investigate the intermolecular effects of the enzyme on the dynamics of the structural-based inhibition and kinetics of the mechanism-based inhibition. In both cases, an in-house Fortan90-based EDA code was employed to calculate the nonbonded intermolecular interaction energies.[174−176] Due to performing the EDA on the metabolite-bound precatalytic structures of each inhibitor, the analysis was run on 12500 snapshots of the 500 ns of the MD simulations. The obtained results were then averaged over the three replicates of each system to qualitatively investigate the stabilizing and destabilizing effects of the enzyme's amino acids on the active site's residues during the noncovalent inhibition. The total difference in the nonbonded intermolecular interaction energy between the selected residues of the active site (termed as the QM region below) and the protein environment during the MD simulation, $\Delta E_{\mathrm{NB}}^{\text{pre-cat}}$, can be calculated as

$$\Delta E_{\mathrm{NB}}^{\mathrm{pre-cat}} = \langle E_{\mathrm{NB}}^{\mathrm{pre-cat}} \rangle_{\mathrm{XO-inhibitor}} - \langle E_{\mathrm{NB}}^{\mathrm{pre-cat}} \rangle_{\mathrm{Apo-XO}} \quad (1)$$

where $\langle E_{\mathrm{NB}}^{\text{pre-cat}} \rangle_{\text{XO-inhibitor}}$ and $\langle E_{\mathrm{NB}}^{\text{pre-cat}} \rangle_{\text{Apo-XO}}$ represent the average of nonbonded intermolecular interactions between the selected residues and each residue of the MM environment for the XO−inhibitor system and the apo-XO, respectively, over the ensembles where the dynamics are sampled.

Due to performing the EDA on the catalytic reactions, i.e., reactant−TS pathway, the analysis was applied to the QM/MM-optimized structures of the reactant and the approximate TS of each system to study the stabilizing and destabilizing effects of the amino acids on the kinetics of the inhibition reaction. MD-simulated trajectories of each hydroxylation step

Scheme 2. Catalytic Hydroxylation Reactions of the FYX-051, 2-Hydroxy-FYX-051, and Dihydroxy-FYX-051 by the XO at the Moco Center

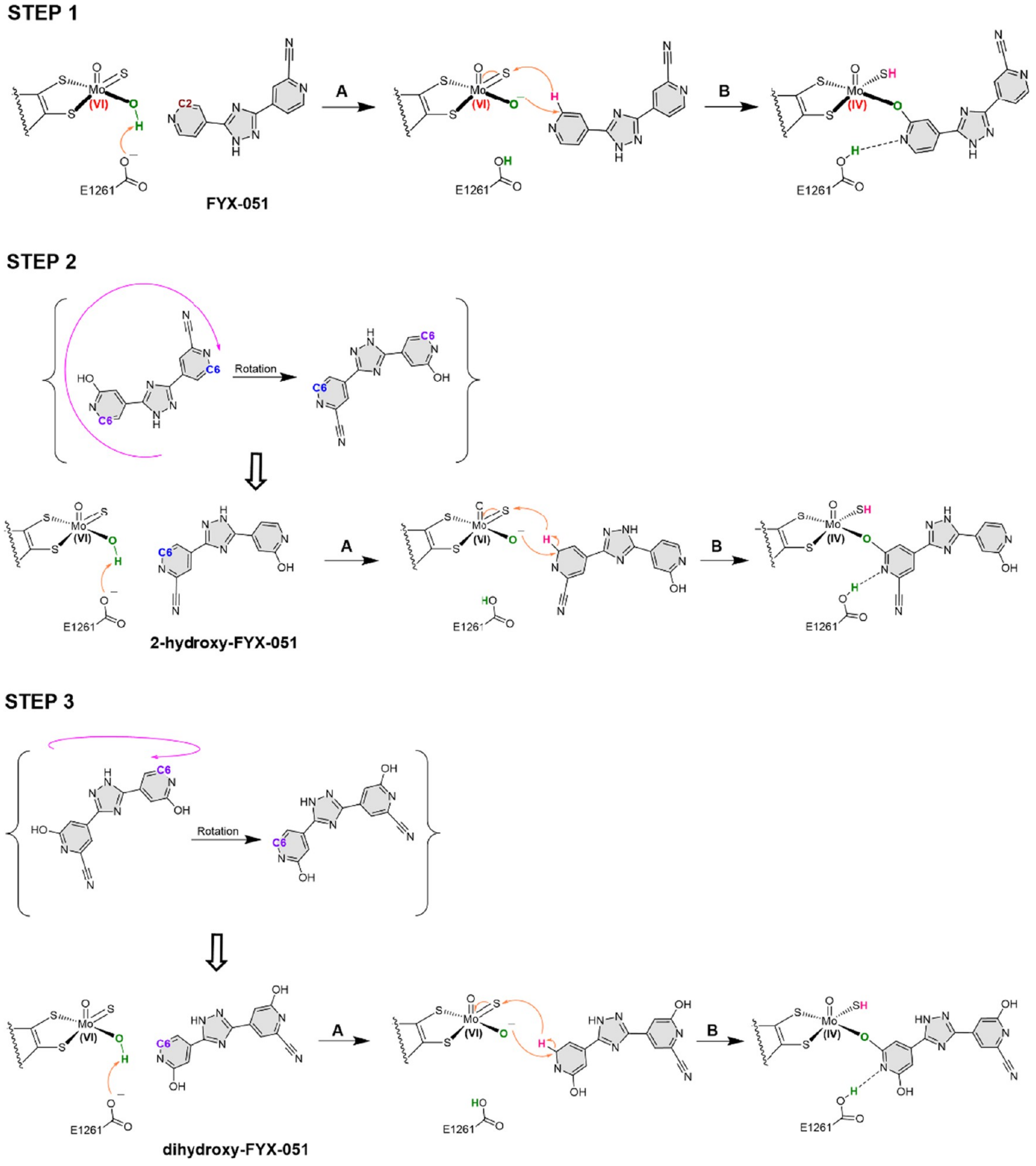

were used by considering the changes in Coulomb and van der Waals interaction energies between the QM subsystem and the residues of the MM region when the system goes from the reactant to the TS. In all cases, in addition to the optimized coordinates, the calculated ESP charges of the QM region (QM atoms and pseudobond atoms) were employed and transferred to the new topology files by the AMBER's ParmEd module[177] for further MD simulations with restraints on the QM region. 10 ns of MD simulation with a 50 kcal mol^{-1} $Å^{-2}$ restraint on the QM atoms was performed at a temperature of 310 K via NVT ensemble. A 10 Å cutoff for nonbonded interactions via the smooth particle mesh Ewald method was set for the long-range Coulomb interactions. SHAKE was employed to handle bonds involving hydrogen atoms. The CPPTRAJ module was used to analyze the RMSD and RMSF values of the MD simulations to monitor the stability of the

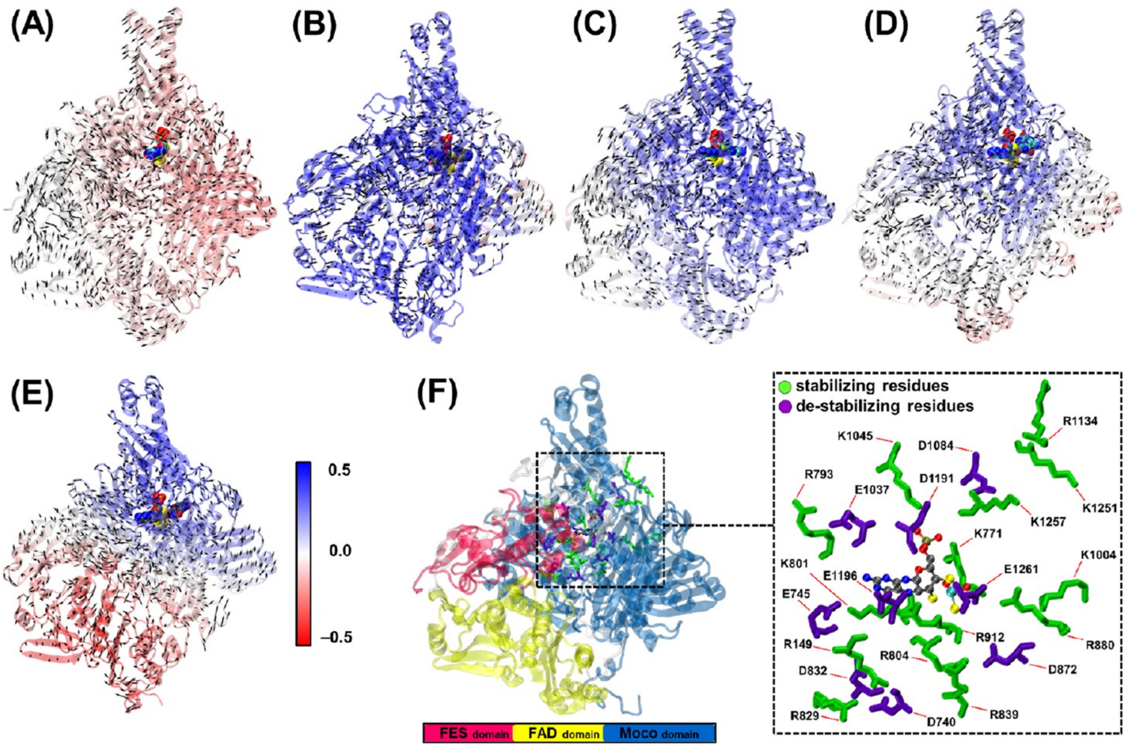

Figure 2. Illustration of the PCA root-mean-square fluctuations and the residue-wise correlation with respect to Moco as a heatmap projected on the protein for (A) apo-XO (B) XO−FYX-051, (C) XO−2-hydroxy-FYX-051, (D) XO−dihydroxy-FYX-051, and (E) XO−trihydroxy-FYX-051. The black arrows point along the direction of the highest-ranked eigenvector (mode 1 in the PCA fluctuation plot), and the amplitude is directly proportional to the length of the arrow. Only fluctuations greater than 1.0 Å are displayed. Areas with correlated movements in the heatmap are colored blue (0.5), noncorrelated areas are white (0.0), and areas with anticorrelated movements are red (−0.5). The first replicate of each MD simulation was used for both the PCA and correlation matrix illustrations. (F) Three-dimensional representation of the residues with considerable nonbonded intermolecular interactions ($|E_{NB}^{pre\text{-}cat}| \geq 35$ kcal mol^{-1}) with the Moco residue of the XO−FYX-051 system (FYX-051 is omitted for clarity). Residues in the sticks have stabilizing (green) and destabilizing (purple) interactions with the Moco shown in ball-and-sticks.

reactant and the TS during the restrained-MD simulation (Figures S22 and S23). The total difference in the nonbonded intermolecular interaction energy between the QM region and the MM environment during the reactant−TS pathway, ΔE_{NB}^{cat}, can be calculated as

$$\Delta E_{NB}^{cat} = \langle E_{QM/i,\,MM}^{TS} \rangle - \langle E_{QM/i,MM}^{reactant} \rangle \qquad (2)$$

where $\langle E_{QM/i,MM}^{TS} \rangle$ and $\langle E_{QM/i,MM}^{reactant} \rangle$ represent the average of nonbonded intermolecular interactions between the residues of the QM region and each residue of the MM environment (i) of the TS and the reactant structures, respectively. The R code[178] and Python libraries NumPy,[132,133] Matplotlib,[134] and Pandas[135] were used for generating and illustrating the graphs.

3. RESULTS AND DISCUSSION

3.1. Structural Effects of the Incoming Inhibitors. As described before, some amino acid residues of the binding pocket are vital for the catalytic hydroxylation of the substrate by the XO, of which E1261 is shown to participate in the proton transfer step.[46,78,89,93] Nishino and co-workers have demonstrated that the mutagenesis of E1262 (in humans) and E730 (in Rhodobacter capsulatus) to alanine completely abolishes enzyme activity.[89,179] Even in the case of structure-based substrates, the presence of these amino acids is of high importance.[42,45,48] It is also known that XO typically catalyzes the hydroxylation of the carbon atom adjacent to the heterocyclic nitrogen of the inhibitor at the Moco center.[47] The proposed mechanism involves an initial proton transfer from Moco to E1261, followed by a nucleophilic attack of the Moco to the substrate (here FYX-051 and its metabolites) and the Moco−substrate complexation (see steps A and B in Scheme 2). Thus, suitable distances between these entities are necessary for the reaction to occur.

Here, we study the effects of the FYX-051 and its hydroxylated metabolites and compare the changes with the apoenzyme. Our MD results show that the presence of the substrate is necessary for the enzyme to keep its active-state conformation at the reaction center. Results of the MD simulations for the apoenzyme show that the Moco and E1261 move away from each other as the simulation time elapses (see Figures S3−S5). The distances between the hydrogen atom of Moco's hydroxide ligand and oxygen atoms of E1261 are around 2−3 Å in the XO−inhibitor structures, while the distances considerably increase to 6−8 Å in the apoenzyme during the simulation. Unlike the apo-XO, the Moco, E1261, and all of the inhibitors in each system remained at reasonable distances for the proton transfer and complexation during the simulation (see Figures S6−S17).

The residue-wise correlation analyses with respect to Moco as a heatmap projected on the protein structure are shown in Figure 2A−E. It can be observed in Figure 2A that the movements of FES and FAD domains are noncorrelated in the apo-XO, while the Moco domain's movements are mostly anticorrelated. Interestingly, upon binding the first metabolite, FYX-051, the motions of nearly all of the domains become correlated with respect to Moco (Figure 2B). As the

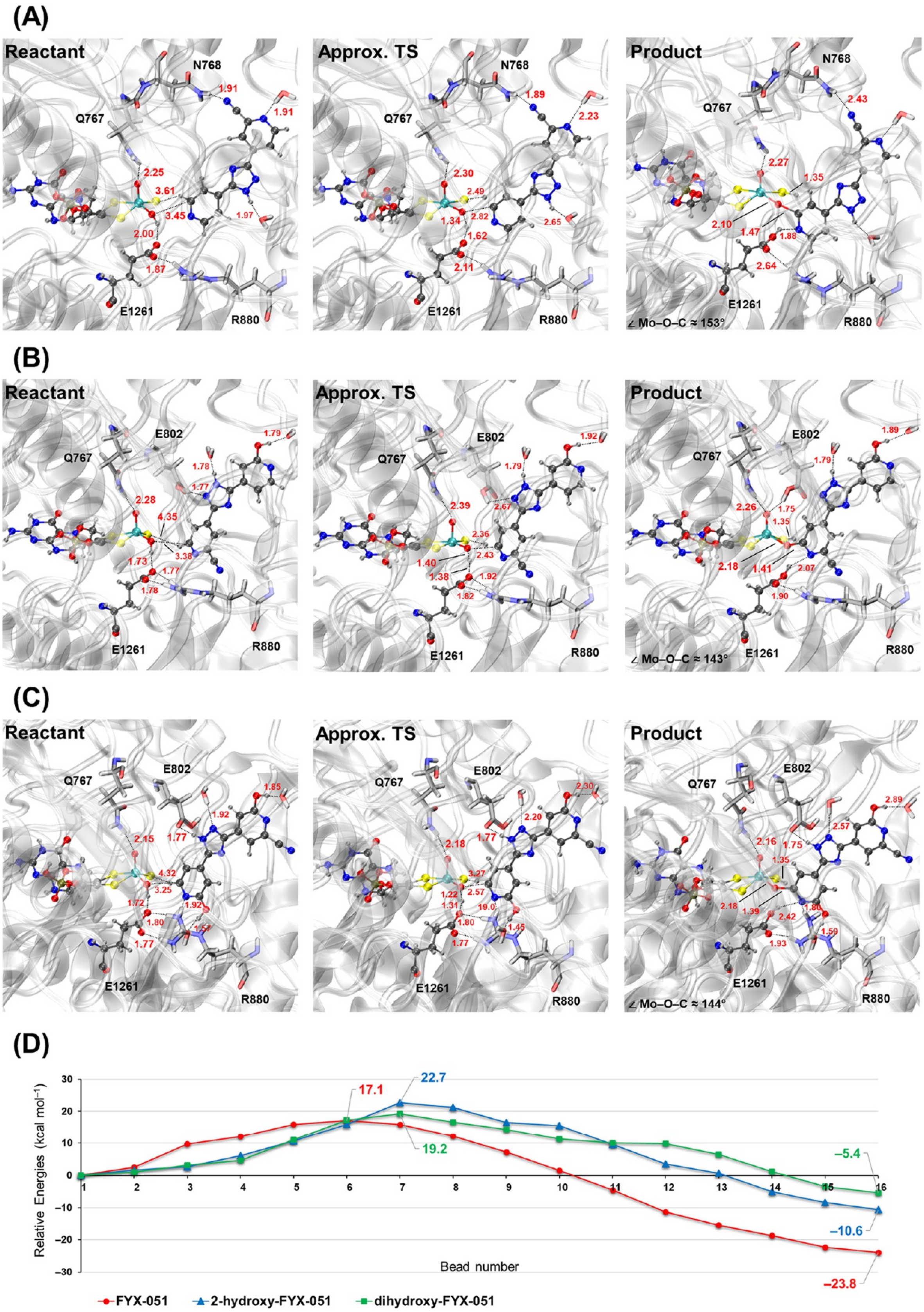

Figure 3. Optimized geometries of the reactant, approximate transition state (Approx. TS), and the product of the complexation reaction of Moco with (A) FYX-051, (B) 2-hydroxy-FYX-051, and (C) dihydroxy-FYX-051. Selected distances and corresponding values (Å) are shown as black dashed lines and red labels. The Moco, E1261, and FYX-051, directly involved in the reaction, are shown as ball-and-sticks, while all of the other important residues in the binding pocket are illustrated as sticks on a ribbon model background of the protein. (D) The minimum energy path for the reduction half-reaction of each system modeled by the QSM. The QM/MM optimization energies are calculated at the ωB97X-D/def2-SVP level of theory with the AMBER ff14SB Force Field.

hydroxylation proceeds to the second metabolite, 2-hydroxy-FYX-051, some parts of the FES and FAD domains become noncorrelated; however, the Moco domain remains correlated (Figure 2C). For the third metabolite, dihydroxy-FYX-051, the FAD domain and some parts of the Moco domain become anti- and noncorrelated (Figure 2D). Finally, in the XO−trihydroxy-FYX-051 system, the FES domain becomes mostly noncorrelated, while the FAD domain becomes completely anticorrelated. However, the Moco domain residues remain correlated with the molybdenum cofactor, except for the regions neighboring the FAD domain, which become noncorrelated (Figure 2E). By proceeding with the hydroxylation, the XO−inhibitor seems to become more similar to the apo-XO, except for the Moco domain's movements, which are considerably correlated to Moco in the presence of the inhibitors.

The EDA analysis for all of the systems (apo-XO and XO−inhibitor) in Figure 2F shows that most of the residues around the active site have negative values of nonbonded interaction with the Moco, suggesting stabilizing effects of the protein residues around the active site on the Moco. The complete graph of the EDA analysis in Figure S24 shows that the total contribution of $E_{\mathrm{NB}}^{\text{pre-cat}}$ between the Moco and the MM environment for all of the studied systems has similar trends along the simulations. The difference in the nonbonded intermolecular interactions ($\Delta E_{\mathrm{NB}}^{\text{pre-cat}}$) between the protein and the Moco considering the apo-XO as a reference suggests that the binding pocket's environment becomes more stabilized by the incoming inhibitors (see Figure S25 and Table S1).

Results of the principal component analysis (PCA) in Figures S3−S17 show that the first two normal modes in all of the structures comprise more than 85% of the movement modes of the systems. Since the first normal mode comprises more than 70% of the movement modes in all of the structures, it was used to interpret the systems (see animations in the Supporting Information). As shown in Figure 2A−E, the directionality of the first normal mode is most similar in the FES and FAD domains of all of the structures. On the other hand, the movements of the Moco domain in XO−2-hydroxy-FYX-051 are similar to the apo-XO, while the other three metabolites are similar to each other. This may suggest that 2-hydroxy-FYX-051 has less stabilizing effects on the Moco domain than the other three metabolites.

3.2. Inhibitor Relative Binding Affinities. Previous experimental results show that after the reduction/oxidation half-reactions, the hydroxylated FYX-051 undergoes a second hydroxylation by XO. Similar to FYX-051, 2-hydroxy-FYX-051 performs time- and concentration-dependent inhibitions. However, a relatively large amount of this metabolite is needed to achieve a potent inhibition ($K_i = 1.5 \times 10^{-6}$ M and $K_i' = 9.2 \times 10^{-6}$ M), which is suggested to be related to the lower binding affinity of 2-hydroxy-FYX-051 for the enzyme.[47] Since the experimental inhibition constants (K_i) are related to the whole reaction, it is not clear whether the necessity of using a relatively large amount of 2-hydroxy-FYX-051 to achieve potent inhibition is due to the lower binding affinity of this metabolite to the active site (chemistry step) or it is related to other steps of the inhibition process. Moreover, the binding affinities and the inhibition constants of the further metabolites, i.e., dihydroxy-FYX-051 and trihydroxy-FYX-051, have not been studied and need more clarification.

The relative binding affinities of each metabolite with respect to FYX-051 were estimated by calculating the relative binding enthalpies between each substrate and the XO enzyme using MM/GBSA. Calculated values of the relative binding affinities (including individual components) are reported in Table S2. The relative ΔH_{bind} values with respect to FYX-051 show that dihydroxy-FYX-051 has the largest relative binding affinity, −4.88 kcal mol^{-1}, with the corresponding values of ΔH_{bind} for 2-hydroxy-FYX-051 of −2.64 and −0.18 kcal mol^{-1} for trihydroxy-FYX-051. Interestingly, the calculated relative binding enthalpies show larger affinities for the first two metabolites compared with FYX-051, suggesting a possible explanation for the driving force for the changes in orientation, which will be further discussed below.

3.3. Catalytic Hydroxylation Reactions. The proposed reaction mechanism by Nishino and co-workers[46] for the hydroxylation reaction of FYX-051 by the XOR at the Moco center (STEP 1 in Scheme 2) is similar to the hydroxylation of the natural substrates (hypoxanthine or xanthine) proposed by Yamaguchi et al.[89] and Metz and Thiel[78,93] (see Scheme 1A). Based on this mechanism, a proton transfer from Moco occurs to E1261 (step A). Subsequently, the negatively charged oxygen of the Moco performs a nucleophilic attack on the C2 carbon of FYX-051 (adjacent to N) with a concomitant hydride transfer to the sulfur, which reduces Mo(VI) to Mo(IV) and a Mo−O−C2 bond forms (step B).

Since the first hydroxylation occurs at the C2-position of the pyridine ring, two different positions are available for the second hydroxylation: the C6-position of the pyridinecarbonitrile ring or the C6-position of the hydroxypyridine (STEP 2 in Scheme 2). LC/MS analysis results have shown that the second hydroxylation occurs at the former position.[47] For the second hydroxylation to occur at this position, it seems more likely that 2-hydroxy-FYX-051 leaves the active site and reenters the binding pocket with its pyridinecarbonitrile ring. After entering the active site, the complexation reaction can be similar to FYX-051, in which the hydrogen of the hydroxyl ligand transfers to E1261, followed by the formation of Mo−O−C6 bridge (adjacent C to N) and Mo−S−H bond between the Moco and the inhibitor.

Similar to the previous step, since the second hydroxylation occurred at the C6-position of the pyridinecarbonitrile ring, the last hydroxylation step occurs at the C6-position of the hydroxypyridine (STEP 3 in Scheme 2). LC/MS analysis also shows that the third hydroxylation occurs at the mentioned position.[47] Similar to 2-hydroxy-FYX-051, for the third hydroxylation to occur, it seems more likely that the dihydroxy-FYX-051 has to leave the active site and reenters the binding pocket but with its hydroxypyridine ring. After entering the active site, the complexation reaction can be similar to the previous steps. It is suggested that the proton transfers from the hydroxyl ligand to E1261, followed by the formation of XO−dihydroxy-FYX-051 complex via a Mo−O−C6 bridge and hydrogen and charge transfer to the Moco.

Herein, we studied the mechanism of the reduction half-reaction pathway of all three metabolites along with the optimized structures of the reactant, product, and the approximate TS (see Figure 3). The calculated values for the Mo−O−C2 angle and Mo−O and O−C2 in the XO−FYX-051 complex are 153°, 2.10 Å, and 1.47 Å, respectively (Figure 3A). These values agree with the experimental ones observed in the 1V97 crystal structure (152°, 2.07 Å, and 1.37 Å, respectively). The RMSD of the active site's atoms and the RMSD of the backbone atoms of the protein in the product with respect to the crystal structure are 1.5 and 3.4 Å, respectively. It can also be seen that E1261 is hydrogen-bonded to Moco's hydroxyl ligand and R880 in the reactant. After the proton transfer, the protonated E1261 makes a new hydrogen bond to the substrate yet maintains its hydrogen bond with R880 and N768. Geometries of the optimized structures also show that in addition to the new hydrogen bond that FYX-051 forms with E1261 (via the nitrogen of its pyridine ring) in the product, it maintains its hydrogen bond with N768 (via its C≡N group) during the reaction, which may help stabilize the product than the reactant.

The reaction path of the second hydroxylation step was investigated to understand if it follows a similar mechanism as for the FYX-051 or a different one. Calculated values for the Mo−O−C6 angle and Mo−O and O−C6 distances in the product are 143°, 2.18 Å, and 1.41 Å, respectively (see Figure 3B), which are close to the respective values in XO−FYX-051. Unlike the FYX-051, 2-hydroxy-FYX-051 is hydrogen-bonded to E802 in the reactant, while the amino acid turns its −OH head to the oxo ligand of the Moco in the product. In the reactant, both carboxylic oxygen atoms of the E1261 are hydrogen-bonded to R880, while in the product, it maintains one of its hydrogen bonds with R880 and forms a new hydrogen bond with the substrate. The OH of the hydroxypyridine ring and the C≡N of the pyridinecarbonitrile ring are both hydrogen-bonded to water molecules of the solvent.

Calculated values for the Mo−O−C6 angle and Mo−O and O−C6 distances in the XO−dihydroxy-FYX-051 complex are 144°, 2.18 Å, and 1.39 Å, respectively (see Figure 3C), which are close to the same values in the products of the previous steps. In the reactant, the substrate is hydrogen-bonded to E802 and R880, while E1261 has hydrogen bonds with Moco's hydroxyl ligand and R880. After the complexation in the product, in addition to its previous hydrogen bonds, the substrate forms a new hydrogen bond with E1261. At the same time, it also has other hydrogen bonds via its two hydroxyls and nitrile groups to water molecules of the solvent.

Experimental values of the k_{cat} for the hydroxylation of the natural substrates by the XOR are 10−16 and 30 s^{-1} for hypoxanthine[89,180] and 7−18 s^{-1} for xanthine[83,84,86−89,181] corresponding to $\Delta G^{\ddagger} \sim 15.4$−16.8 and ~ 15.8−16.3 kcal mol^{-1}, respectively. Calculated QM/MM barrier energies for the reduction half-reaction from two exhaustive studies by Metz and Thiel[78] and Cerqueira and co-workers[95] are 10−18.3 kcal mol^{-1} (different setups) and 16.9 kcal mol^{-1}, respectively. Calculated reaction free energy by the earlier study differs from −9.3 to 4.9, while the latter study showed that the complexation occurs in two sequential steps with ΔG_R of 11.7 and −8.5 kcal mol^{-1}. An experimental study by Spector et al. on the inhibition of XO with oxipurinol, a competitive-type inhibitor of this enzyme, showed that the K_i of the inhibition reaction is 1.8 min^{-1} ($\Delta G^{\ddagger} \sim 31.0$ kcal mol^{-1}) and 1.4 min^{-1} ($\Delta G^{\ddagger} \sim 28$ kcal mol^{-1}) for human and bovine enzymes, respectively.[85] Although the barrier energy for oxipurinol is around double the value for xanthine, it is shown to be an ideal mechanism-type inhibitor of the XO. As mentioned before, the K_i values for the XOR inhibition by the FYX-051 are 2 orders of magnitude smaller than that of allopurinol (5.7×10^{-9} and 7.0×10^{-7} M, respectively). However, these results are related to the noncovalent inhibition, not the chemistry step, i.e., the reduction half-reaction.

Our QM/MM results show that the complexation reaction between XO and FYX-051 is exoergic with a reaction energy and barrier energy of −23.84 and 17.12 kcal mol^{-1}, respectively (red trace in Figure 3D). In the approximate TS, the hydroxyl ligand's proton is transferring to E1261, while the Mo−O···C2 and Mo═S···H-bonds are forming in a tetrahedral geometry of the metal center. These results suggest that FYX-051 can act as a competitive inhibitor of XO and might be a more efficient inhibitor than oxipurinol. The blue trace in Figure 3D shows that the second hydroxylation step is also exoergic with the reaction energy and the barrier energy of −10.61 and 22.70 kcal mol^{-1}, respectively. As can be seen, the approximate transition state of the XO−2-hydroxy-FYX-051 complex is similar to the TS of the first step but ~5.6 kcal mol^{-1} more endergonic than that for XO−FYX-051. This might be the reason (or at least one of the reasons) for the larger experimental inhibition constant (K_i) of the 2-hydroxy-FYX-051.

The third hydroxylation step is also exoergic with a similar TS to the previous steps and the reaction and barrier energies of −5.43 and 19.19 kcal mol^{-1}, respectively (green trace in Figure 3D). The approximate TS of the XO−dihydroxy-FYX-051 complex is ~2.1 kcal mol^{-1} larger than that for XO−FYX-051, while ~3.5 kcal mol^{-1} lower than that for XO−2-hydroxy-FYX-051. Moreover, the XO−dihydroxy-FYX-051 complex is around 5.2 kcal mol^{-1} less stable than the XO−2-hydroxy-FYX-051 complex. These differences in the barrier and reaction energies might be one of the reasons for the quick conversion of the dihydroxy-FYX-051 to trihydroxy-FYX-051, as seen in the experimental results.

3.4. Characterization of the Mo Reduction Pathway during Hydroxylation Catalysis.

Experimental studies on the XOR inhibition by xanthine[83,86] and FYX-051[46] have proposed that the negative charge responsible for the reduction of Mo(VI) to Mo(IV) is transferred via a H^- ion,[182] which is computationally believed to be the rate-limiting step of the XO−xanthine reduction reaction.[78,92−94] However, in some studies on xanthine or other substrates like formaldehyde, acetaldehyde, formamide, and formamidine, the activation barriers for this step, i.e., transfer of a hydride ion to a sulfido ligand, are excessively high ($\Delta E \geq 30$ kcal mol^{-1}) and not catalytically feasible.[91,92,94,96−98] Since the complexation reaction involves transferring a proton and two electrons, three mechanisms are plausible: the hydride transfer mechanism, in which the H and two electrons are directly transferred to the sulfido ligand of the Moco. In the second mechanism, the hydrogen is transferred as a proton, and a pair of electrons are transferred via the oxo-bridge. Finally, the third mechanism consists of a hydrogen atom transfer to the sulfido group, while the second electron is transferred via the oxo-bridge. Each of these mechanisms reflects a specific electrostatic potential charge in the reaction's transition state.

A topological and population analysis was employed to investigate the electronic structure of the critical points along the reaction pathway to investigate which of the above-mentioned mechanisms seems more probable in the studied hydroxylation reactions. The changes in the electrostatic potential charges (ESP) and the electron localization functions (ELFs) were calculated for the hydroxylation of each metabolite. According to the calculated electrostatic potentials along the hydroxylation reactions, the transferring hydrogen is almost neutral at the transition state (see Figure S26). An exhaustive study by Cerqueira and co-workers[95] on the catalytic mechanism of XO with its natural substrate, xanthine, showed similar results, suggesting that the transfer occurs via a

Scheme 3. Proposed Mechanism for the Final Step of the XOR Inhibition by Trihydroxy-FYX-051 at the Moco Center

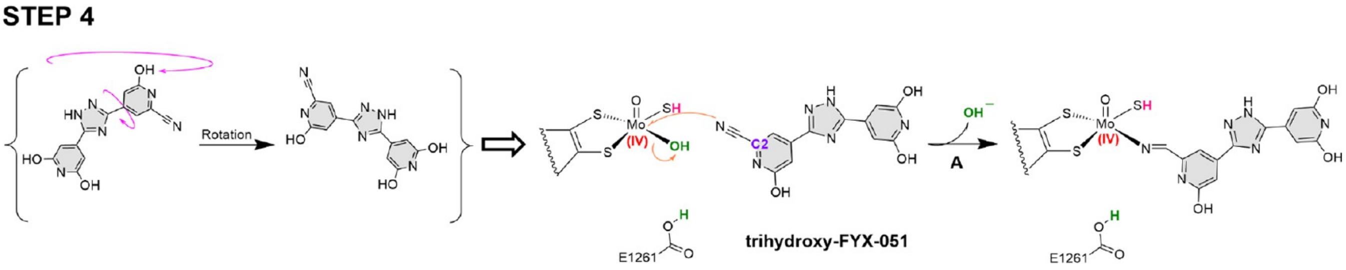

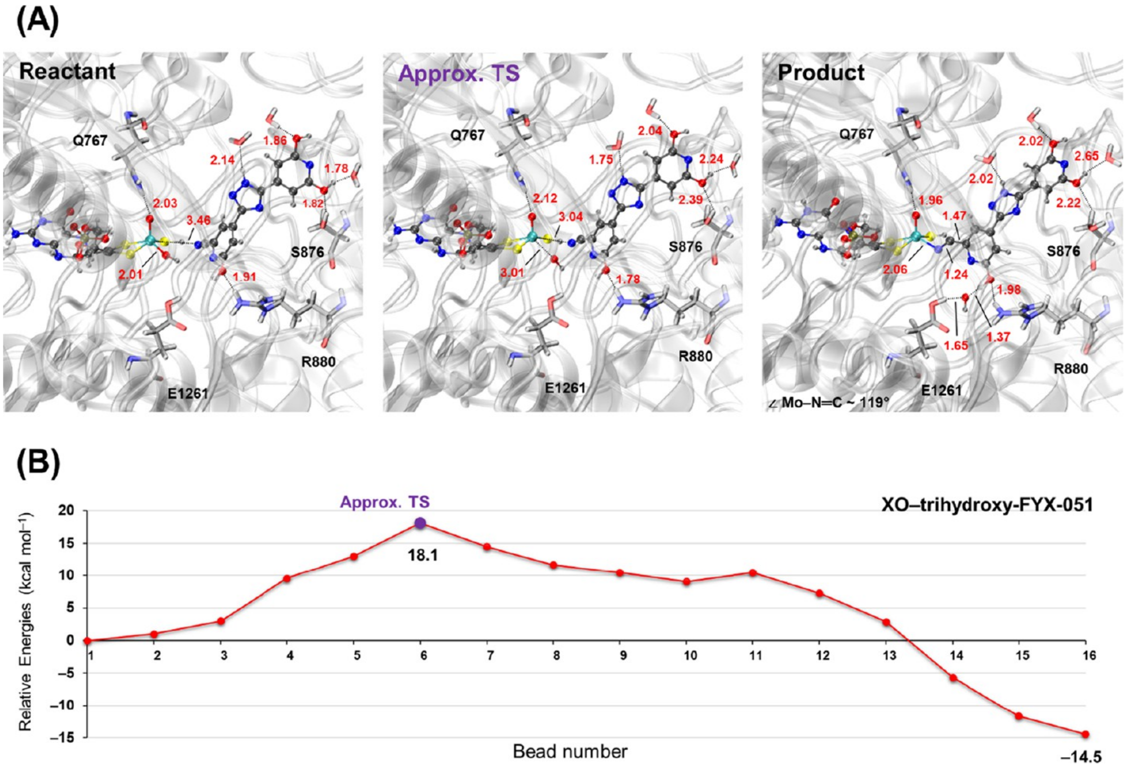

Figure 4. (A) Optimized geometries of the reactant, approximate transition state (Approx. TS), and the product of the binding reaction between XO and trihydroxy-FYX-051. Selected distances and corresponding values (Å) are shown as black dashed lines and red labels, respectively. The Moco and trihydroxy-FYX-051 are shown as ball-and-sticks, while all of the other important residues of the binding pocket are illustrated as sticks on a ribbon model background of the protein. (B) The minimum energy path for the complexation modeled by the QSM. The QM/MM optimization energies are calculated at the ωB97X-D/def2-SVP level of theory with the AMBER ff14SB Force Field.

"hydrogen−one electron-coupled mechanism", which is consistent with the third plausible mechanism discussed above. Moreover, a computational study[183] by Kirk and co-workers on purine- and nonpurine-based substrates and a hybrid spectroscopic/electronic structure study[184] by them on aldehyde substrate revealed that the hydrogen of C−H for all their studied XO substrates is transferred to the terminal sulfido at the transition state with a near-neutral (or slightly positive) charge. Calculated ELF basins in Figure S27 and Table S4 show the formation of Mo−S−H and Mo−O−C trisynaptic basins during the reactant−TS−product pathway in all three systems (electron population ≈ 1.0−1.2e$^-$). Taken together, these results suggest that the hydroxylation reaction steps occur via the third proposed mechanism.

3.5. XO−Trihydroxy-FYX-051 Complexation (Final Step).

Nishino and co-workers[47] showed that the product of the last hydroxylation step, i.e., trihydroxy-FYX-051, acts as the final inhibitor of XO. Like oxipurinol, the substrate in this structure is directly coordinated with the molybdenum atom via the nitrile nitrogen of the ligand. It is believed that both the trihydroxy-FYX-051 and oxipurinol coordinate with the reduced cofactor during the enzymatic turnover, in which the molybdenum is still in its (IV) oxidation state.[159] Thus, the final inhibition reaction by the oxipurinol[34,80] and trihydroxy-FYX-051[119,159] seems to occur before the oxidation half-reaction and enzymatic turnover are completed.

As discussed in the previous section, the final hydroxylation occurs at the C6-position of the hydroxypyridine leading to the formation of trihydroxy-FYX-051. To form the XO−trihydroxy-FYX-051 complex via the C≡N group, it seems more likely that the substrate leaves the active site and reenters the binding pocket with its hydroxypicolinonitrile ring facing the Moco. The proposed mechanism for the complexation between XO and trihydroxy-FYX-051 suggested by Nishino and co-workers[119] is given in Scheme 3, in which the water-exchangeable OH ligand of the reduced molybdenum (Mo^{+4}) is replaced by the nitrogen atom of trihydroxy-FYX-051 to form a stable complex (step A).[119] Furthermore, a nucleophilic

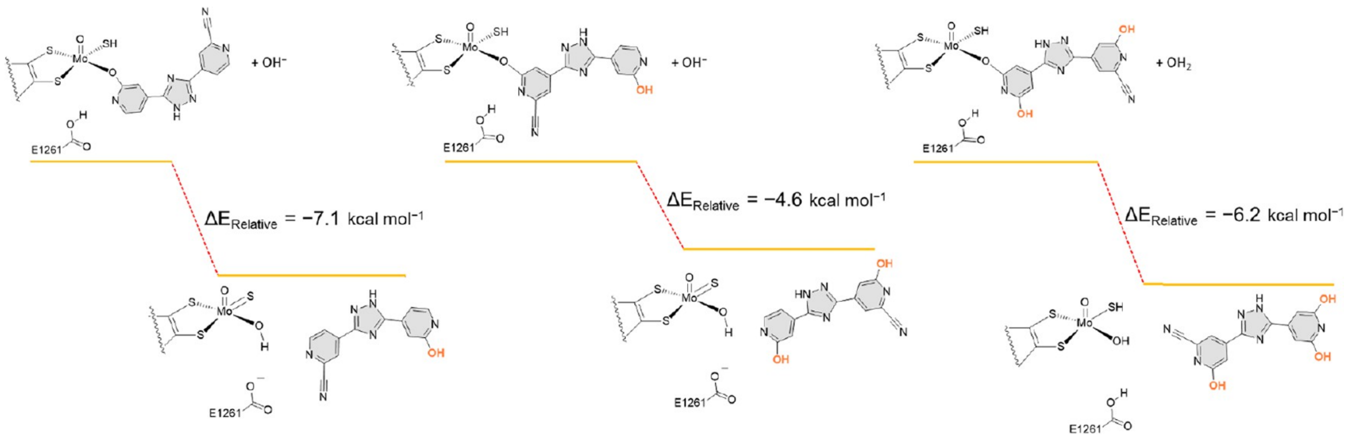

Figure 5. Calculated QM/MM relative energies for individual metabolites in consecutive reaction steps.

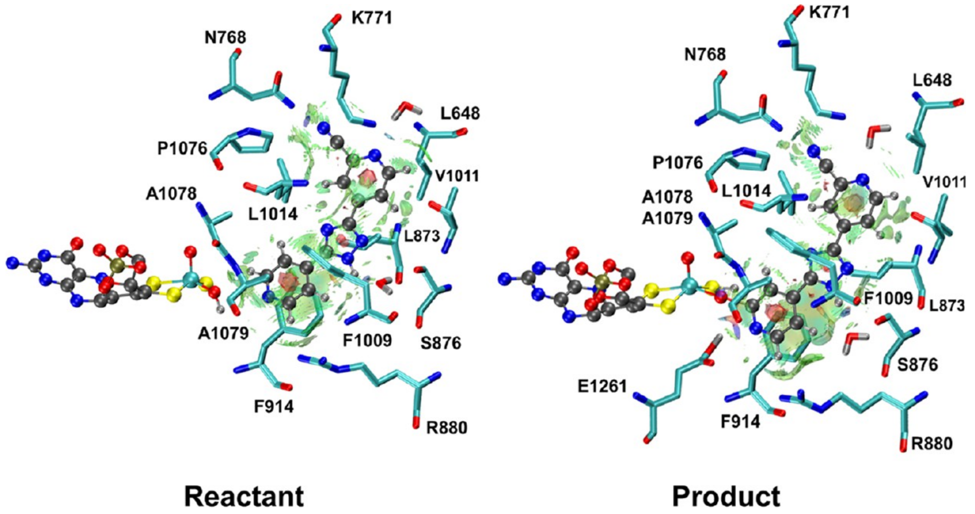

Figure 6. Plots of the noncovalent interactions (NCIs) between the substrate and the surrounding residues in the reactant and product of XO−FYX-051. The isovalue for the NCI visualization is 0.4 with a color scale of −0.05 a.u. < sign(λ_2)ρ < 0.05 a.u. The Moco and the substrate are illustrated in ball-and-sticks, while the amino acids and water molecules are given in sticks. The protein chain and H atoms of the Moco and amino acids are not shown for clarity.

attack by the OH^- breaks down the complex, and the molybdenum is reoxidized to its initial oxidation state (Mo^{+6}) by proton/charge transfer (this step is not shown in the scheme).

The QM/MM-optimized geometries of the critical structures during the complexation reaction are given in Figure 4A. Calculated values for the Mo−N═C and N═C−C2 angles and Mo−N, N═C, and C−C2 distances in the XO−trihydroxy-FYX-051 complex are 119°, 138°, 2.06 Å, 1.24 Å, and 1.47 Å, respectively. These values are in good agreement with the experimental values in PDB 3AM9 of 111°, 127°, 2.14 Å, 1.06 Å, and 1.61 Å, respectively. The RMSD of the active site's atoms and the RMSD of the backbone atoms of the protein in the product with respect to the crystal structure are 1.1 Å and 3.2 Å, respectively. It can also be seen that in the reactant, trihydroxy-FYX-051 is H-bonded to R880, Ser876, and three water molecules, which are observed to remain after the complexation. Furthermore, in the product, Moco's exchangeable hydroxyl is placed between E1261, R880, and the hydroxyl group of the substrate and is stabilized by forming two hydrogen bonds with the substrate and E1261. As shown in Figure 4A (middle), in the approximate TS, the Mo···OH bond breaks, while the Mo···N≡C bond forms, and the N≡C−C2 angle changes to ∼165°. It should be mentioned that based on the experimental results,[47] the substrate has hydrogen bonds with R880 and E802 in its bound form, while in our optimized product, trihydroxy-FYX-051 forms H-bonds with R880, Ser876, and three water molecules.

Based on the QM/MM optimization results in Figure 4B, the product of the XO−trihydroxy-FYX-051 complexation is 14.47 kcal mol^{-1} more stable than the reactant, and the energy barrier is 18.09 kcal mol^{-1}. There is no experimental K_i for the inhibition of XO by trihydroxy-FYX-051. However, as mentioned before, the corresponding value for the inhibition by oxipurinol, which might have a similar mechanism (see Scheme 1D), is ∼28−31 kcal mol^{-1}. Our calculated energy barrier is ∼10−13 kcal mol^{-1} less endergonic than the oxipurinol. This might come from factors such as more stabilizing contributions between the enzyme and the TS and the number of noncovalent interactions between the trihydroxy-FYX-051 and the binding pocket's residues during the reaction, which are discussed below.

As discussed previously, the calculated $\Delta H_{\text{bind}}^{\text{relative}}$ for the consecutive metabolites provides a possible explanation for the driving force of the reorientation. This is further supported by the calculated relative QM/MM energies for the individual

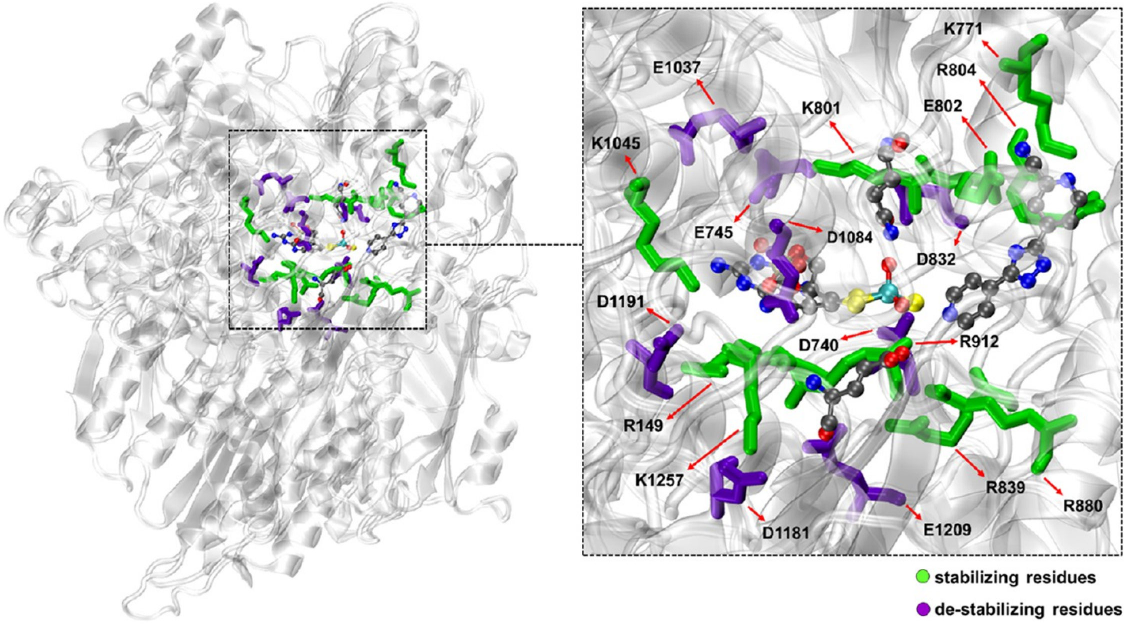

Figure 7. Three-dimensional representation of the residues with considerable nonbonded intermolecular interactions ($|E_{\mathrm{NB}}^{\mathrm{MD}}| \geq 60$ kcal mol^{-1}) with the active site of the XO−FYX-051. Residues in the sticks have stabilizing (green) and destabilizing (purple) interactions with the active site (in ball-and-sticks) on a ribbon model background of the protein. The same residues with slightly different intermolecular interactions were seen for the other metabolites.

metabolites in the sequential steps. The calculated $\Delta E_{\mathrm{relative}}$ values in Figure 5 show that the reactant for the respective metabolite of each step is more stable than the product of the corresponding metabolite in the previous step. These results are consistent with the calculated relative binding affinities above, suggesting that the metabolites' reorientation is energetically favorable to drive the reaction forward (detailed results in Table S4). Based on the comparative similarity in relative binding affinities and relative QM/MM energies for the different metabolites, the larger amount of 2-hydroxy-FYX-051 needed for *in vitro* inhibition may be related to the nonchemistry steps of the inhibition reaction or the higher energy barrier of the hydroxylation reaction.

3.6. Noncovalent Interactions between the XO and Studied Inhibitors. As mentioned before, unlike allopurinol, FYX-051 also behaves as a structure-based inhibitor and blocks the substrate channel by forming interactions with the surrounding amino acids. Some residues were found in the crystal of the XOR−FYX-051-bound structure, including N768, E802, F914, F1009, and E1261.[46] However, these interactions are related to the structure of the XO−FYX-051 and do not provide much information about the noncovalent interactions between the inhibitor and the residues of the active site before the complexation, i.e., structure-based inhibition characteristics of the FYX-051. Plots of the noncovalent interactions (NCIs) in Figure 6 illustrate the binding pocket's residues having interacting surfaces with FYX-051. It can be seen that in addition to the mentioned residues in the experimental studies, several other residues such as L648, K771, L873, S876, R880, V1011, and L1014 and various water molecules have weak and strong attraction interactions (in the NCI scale) with the substrate before and after the complexation.

These interactions help stabilize the inhibitor in the binding pocket and help explain the structure-based inhibition by the FYX-051. The NCI surfaces for the other three metabolites in Figure S28 show slight changes; however, based on the detailed results in Table S5, there is no significant difference between the noncovalent interactions of the studied metabolites with the residues of the active site. This may explain why the binding affinities between all of the substrates and the XO are not considerably different. Moreover, several residues with NCIs are common between all of the metabolites, i.e., L648, E802, L873, R880, F914, F1009, L1014, P1076, A1078, and A1079. Many of these residues were seen in a study by Nishino and co-workers[185] on the structure-based inhibition of mammalian and bacterial XOR by febuxostat, which is one of the best noncovalent inhibitors of XOR and administered to patients worldwide. This might be the reason for the high structure-based inhibition potential of the FYX-051 metabolites.

Another helpful tool to evaluate the contributions of the enzyme's residues to the active site is analyzing the intermolecular interactions between individual residues and the different metabolites using energy decomposition analysis (EDA). This analysis can be used as a qualitative indicator to facilitate the understanding of the electrostatic effects of the enzyme's environment on either the MD simulation or the QM/MM reaction pathway. The three-dimensional arrangements of the amino acids in Figure 7 show that the residues with significant nonbonded contributions are concentrated around the active site. Our EDA on the metabolite-bound precatalytic structures suggests that the active site experiences similar intermolecular interactions with the enzyme's residues in all of the metabolites (more details in Figure S29 and Table S6), which is consistent with the binding enthalpies and the NCIs show that the environmental effects of the enzyme are not considerably different from the studied metabolites.

EDA was also performed on the reactant and TS's structures along each metabolite's reactant → TS step. The calculated graphs of the per-residue intermolecular interaction energy differences ($\Delta E_{\mathrm{NB}}^{\mathrm{cat}}$ in eq 2) between the reactant and TS of all

https://doi.org/10.1021/acscatal.3c01245
ACS Catal. 2023, 13, 6023−6043

of the XO−inhibitor systems are given in Figure S30, and detailed results are listed in Table S7. These results suggest that significant nonbonded interactions mostly come from residues located in the Moco and FES domains, while the FAD domain does not contribute considerably to stabilizing or destabilizing the catalytic reaction. Therefore, the sum of the nonbonded interactions can be a relatively good approximation of the environmental effects of the enzyme on the reactant−TS pathway.[186] The sum of the nonbonded interactions $(\sum \Delta E_{\mathrm{NB}}^{\mathrm{cat}})$ for the reactant−TS pathways in XO−FYX-051, XO−2-hydroxy-FYX-051, XO−dihydroxy-FYX-051, and XO−trihydroxy-FYX-051 are −20, 12.3, −2.8, and −17.0 kcal mol^{-1}, respectively (see Table S7). This suggests that the enzyme environment stabilizes the TS of XO−FYX-051 and XO−trihydroxy-FYX-051, thus favoring the complexation reaction for these two systems. For the XO−dihydroxy-FYX-051 system, the protein appears to provide only slight stabilization to the TS. By contrast, the TS associated with the reaction for the XO−2-hydroxy-FYX-051 system shows destabilizing interactions with the protein environment. Although these results are consistent with the calculated QM/MM barrier energies, results of the nonbonded interactions also show less stability of the TS in the XO−2-hydroxy-FYX-051 system compared to the other three metabolites. More details regarding the orientations and effects of the residues with considerable nonbonded contributions to the reactant−TS pathway of each metabolite are shown in Figure S31.

A study by Nishino and co-workers[89] showed that E802V and R880V mutations considerably abrogate the XO's activity toward hypoxanthine and xanthine, respectively. Their results also showed that, unlike the wild type, the mutants were not subject to time-dependent inhibition by allopurinol. The crystal structure of the E802V mutant showed that the positions and orientations of the residues of the active center are very similar to that in the wild type, indicating that the decrease in the enzymatic activity is not related to the conformational changes. Hille and co-workers also suggested that R880[116,179] and E802[187,188] (R310 and E232 in *R. capsulatus* enzyme) are involved in the transition-state stabilization of XO−xanthine by compensation of negative charge accumulation on xanthine (R880) and proton tautomerization (E802). Another exhaustive study by Scazzocchio and co-workers[189] showed that G799S, R880Q/G, H884Y, N887K, and A1079T mutations lead to a partial or total loss of XO function. They also showed that the mutations in R880 are all unable to accept xanthine or oxipurinol as a substrate. Hiratsuka and co-workers[190] found a deficiency in the XO activity in R149C and T909K mutants, a low XO activity in P554S, R606Q, N908K, and C1317Y mutants, and a high activity in I702V and H1220R mutants. In addition, several clinical studies have been performed on the mutagenesis of XO, in which either the mutations led to xanthinuria (XOR deficiency leading to hypouricemia) or hyperuricemia (higher activity of XOR). Some of these trials on human cases with xanthinuria have reported XO mutants corresponding to R149C,[191] R228T,[192] K721X,[193] R824X,[194] R880X,[194] T909M,[195] R912W,[196] and R1282X.[197]

Investigating the effects of the mutations on xanthine and allopurinol and comparing the results with our nonbonded contributions can provide a good insight into the residues with significant effects on the XO inhibition. This can be used in future studies on designing more efficient drugs with better covalent inhibitory effects and better noncovalent inhibition of the XO by interacting with the candidate residues. Some of the mutated residues in the XO enzyme are located far from the active site, which is not helpful for designing hybrid-type inhibitors. However, according to the detailed results of the precatalytic and catalytic EDAs (in Tables S6 and S7, respectively), many of these mutated residues have a significant stabilizing effect. When these residues were mutated, it caused a partial or total loss of XO function, such as R149, R228, R606, E802, R824, R880, H884, R912, A1079, and R1282. This agreement between the experimental/clinical mutagenesis studies and our findings based on the EDA suggests that the predicted effects of the binding pocket residues can be considered for further hybrid-type inhibitor developments.

As shown earlier, NCI results also suggest several residues of the binding pocket forming noncovalent surfaces (green and blue) with the studied inhibitors. Therefore, by considering the obtained results via the EDA and NCI, it seems that residues L648, K771, E802, R839, L873, R880, R912, F914, F1009, L1014, and A1079 that significantly interact with the studied inhibitors can be considered as potent interacting targets for further hybrid-type inhibitor developments (see Figure 8).

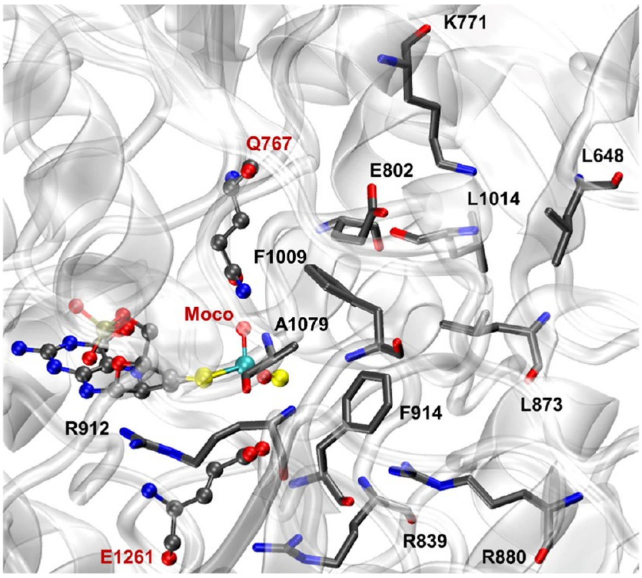

Figure 8. Residues around the binding pocket (in the sticks) with significant noncovalent interactions—stabilizing contributions in EDA and green/blue surfaces in NCI—with the molybdenum cofactor (in ball-and-sticks). Hydrogen atoms are not shown for clarity.

Taken together, our results suggest that topiroxostat can act as a hybrid-type inhibitor. In line with experimental reports by the discoverers of this drug, our insights show the favorability of the sequential hydroxylation of topiroxostat by XO. Various analyses on the precatalytic inhibition not only suggest that the binding pocket's environment becomes more stabilized by the incoming inhibitors but also that the presence of the substrate is necessary for the enzyme to keep its active-state conformation. Several amino acids around the binding cavity play important stabilizing roles via noncovalent interactions during the inhibition process. These results also suggest that in addition to the concentration of the stabilizing residues around the binding pocket, distal nonbonded interactions mostly come from residues of the Moco and FES domains. The kinetics of the catalytic reactions suggests the probable inhibition effects by all of the metabolites and provides a possible explanation for why a relatively larger amount of the first hydroxylated metabolite is needed for a potent inhibition. The mechanistic insights of this study on how the reduction half-reaction occurs and the suggested residues influencing the inhibition can be used to design hybrid-type inhibitors with more structure- and mechanism-based features.

4. CONCLUSIONS

In this study, molecular dynamics (MD) simulations and quantum mechanics/molecular mechanics (QM/MM) optimizations were employed to study the mechanism of the sequential hydroxylation reaction of FYX-051 and its metabolites, 2-hydroxy-FYX-051 and dihydroxy-FYX-051, by the active site of the xanthine oxidase. The complexation reaction between XO and the final hydroxylated metabolite, trihydroxy-FYX-051, which binds to the active site in a different mode, was also investigated. MD simulations showed that the presence of the substrate is essential for the enzyme to keep its active-state conformation at the reaction center. Similar to the proposed hydroxylation mechanism for the hypoxanthine and xanthine, our reaction path optimizations for all three hydroxylation reactions suggest a proton transfer from the Moco to E1261 with a nucleophilic attack by Moco's oxygen to the inhibitor's carbon (adjacent to N). However, the changes in the electrostatic potential charges (ESP) and the electron localization functions (ELFs) suggest that the reduction of Mo(VI) to Mo(IV) occurs via a hydrogen atom transfer to the sulfido group, while the second electron is transferred via Mo−O−C bond's oxo-bridge. In the proposed mechanism for the complexation between XO and trihydroxy-FYX-051, the water-exchangeable OH ligand of Mo(IV) is replaced by the nitrogen atom of trihydroxy-FYX-051 to form a stable complex. The experimental values of K_i for FYX-051 and 2-hydroxy-FYX-051 obtained via steady-state kinetic studies have shown the necessity of a larger amount of the latter metabolite for *in vitro* potent inhibition (5.7×10^{-9} and 1.5×10^{-6} M, respectively). Molecular dynamics simulations and calculated binding enthalpies (ΔH_{bind}) suggest that 2-hydroxy-FYX-051 exhibits a modestly larger relative binding affinity than the other studied metabolites, consistent with the noncovalent (structure-based) inhibition mechanism. Our QM/MM calculations on the reaction mechanisms indicate that 2-hydroxy-FYX-051 has the largest energy barrier compared with the other metabolites, 22.7 kcal mol^{-1} in comparison with 17.1, 19.2, and 18.1 kcal mol^{-1} for FYX-051, dihydroxy-FYX-051, and trihydroxy-FYX-051, respectively (Figures 3D and 4B). These combined results help explain why a relatively larger amount of this inhibitor is needed for a potent inhibition. Calculated QM/MM reaction energies showed that the complexation reactions between the XO and all of the studied metabolites are exergonic. In addition, a comparison between the barrier energies of the studied metabolites and the experimental values of the k_{cat} for XO's natural substrates (hypoxanthine and xanthine) and oxipurinol (the "gold-standard" inhibitor of XO) clearly shows the promising mechanism-based (covalent) inhibitory effects of the studied metabolites. The analysis of the nonbonded interactions between the XO and the studied metabolites and comparing the obtained results with the mutagenesis studies suggested that several residues of the binding pocket with significant nonbonded contributions (L648, K771, E802, R839, L873, R880, R912, F914, F1009, L1014, and A1079) can be considered as potent interacting targets for further hybrid-type inhibitor developments.

■ ASSOCIATED CONTENT

Data Availability Statement

All simulations and analyses employed via third-party software are described and referenced in the Computational Methods section. The EDA and LICHEM software programs are available at the Cisneros Research Group GitHub: https://github.com/CisnerosResearch/AMBER-EDA and https://github.com/CisnerosResearch/LICHEM.

SI Supporting Information

The Supporting Information is available free of charge at https://pubs.acs.org/doi/10.1021/acscatal.3c01245.

Additional details of MD, EDA, NCI, and QM/MM (PDF)

Additional ESI for the initial coordinates and parameters for all of the studied systems (ESI-1.zip) (ZIP)

Videos animating the first principal modes and the reaction paths for each inhibition step (ESI-2.ZIP) (ZIP)

■ AUTHOR INFORMATION

Corresponding Author

G. Andrés Cisneros − *Department of Chemistry and Biochemistry, The University of Texas at Dallas, Richardson, Texas 75080, United States; Department of Physics, The University of Texas at Dallas, Richardson, Texas 75080, United States;* orcid.org/0000-0001-6629-3430; Email: andres@utdallas.edu

Authors

Yazdan Maghsoud − *Department of Chemistry and Biochemistry, The University of Texas at Dallas, Richardson, Texas 75080, United States;* orcid.org/0000-0002-4051-0844

Chao Dong − *Department of Chemistry and Physics, The University of Texas Permian Basin, Odessa, Texas 79762, United States*

Complete contact information is available at: https://pubs.acs.org/10.1021/acscatal.3c01245

Notes

The authors declare no competing financial interest.

■ ACKNOWLEDGMENTS

This study was funded by NIH Grant No. R01GM108583. The computational time for this project was provided by the University of North Texas CASCaM CRUNTCh3 high-performance cluster (partially funded by the NSF Grant Nos. CHE1531468 and OAC-2117247), the NSF Extreme Science and Engineering Discovery Environment, XSEDE (Project No. TG-CHE160044), and the University of Texas at Dallas' Cyberinfrastructure and Research Services, Ganymede and Titan HPC clusters. The authors thank Professor Maria João Ramos for kindly providing the parameters of the molybdenum cofactor.

■ REFERENCES

(1) Pritsos, C. A. Cellular distribution, metabolism and regulation of the xanthine oxidoreductase enzyme system. *Chem. Biol. Interact.* **2000**, *129*, 195−208.

(2) Garattini, E.; Mendel, R.; Romão, M. J.; Wright, R.; Terao, M. Mammalian molybdo-flavoenzymes, an expanding family of proteins: structure, genetics, regulation, function and pathophysiology. *Biochem. J.* **2003**, *372*, 15−32.
(3) Hesberg, C.; Hänsch, R.; Mendel, R. R.; Bittner, F. Tandem orientation of duplicated xanthine dehydrogenase genes from Arabidopsis thaliana: differential gene expression and enzyme activities. *J. Biol. Chem.* **2004**, *279*, 13547−13554.
(4) Yasuhara, A.; Akiba-Goto, M.; Aisaka, K. Cloning and sequencing of the aldehyde oxidase gene from Methylobacillus sp. KY4400. *Biosci. Biotechnol. Biochem.* **2005**, *69*, 2435−2438.
(5) Mendel, R. R. Biology of the molybdenum cofactor. *J. Exp. Bot.* **2007**, *58*, 2289−2296.
(6) Zhang, Y.; Gladyshev, V. N. Molybdoproteomes and evolution of molybdenum utilization. *J. Mol. Biol.* **2008**, *379*, 881−899.
(7) Kurosaki, M.; Bolis, M.; Fratelli, M.; Barzago, M. M.; Pattini, L.; Perretta, G.; Terao, M.; Garattini, E. Structure and evolution of vertebrate aldehyde oxidases: from gene duplication to gene suppression. *Cell. Mol. Life Sci.* **2013**, *70*, 1807−1830.
(8) Garattini, E.; Terao, M. Aldehyde oxidase and its importance in novel drug discovery: present and future challenges. *Expert Opin. Drug Discovery* **2013**, *8*, 641−654.
(9) Marelja, Z.; Dambowsky, M.; Bolis, M.; Georgiou, M. L.; Garattini, E.; Missirlis, F.; Leimkühler, S. The four aldehyde oxidases of Drosophila melanogaster have different gene expression patterns and enzyme substrate specificities. *J. Exp. Biol.* **2014**, *217*, 2201−2211.
(10) Garattini, E.; Terao, M. Xanthine Oxidoreductase and Aldehyde Oxidases. In *Comprehensive Toxicology*, 3rd ed.; Elsevier: Oxford, 2018.
(11) Hille, R.; Nishino, T. Xanthine oxidase and xanthine dehydrogenase. *FASEB J.* **1995**, *9*, 995−1003.
(12) Hille, R. The mononuclear molybdenum enzymes. *Chem. Rev.* **1996**, *96*, 2757−2816.
(13) Rajagopalan, K.; Johnson, J. L. The pterin molybdenum cofactors. *J. Biol. Chem.* **1992**, *267*, 10199−10202.
(14) Romão, M. J.; Archer, M.; Moura, I.; Moura, J. J.; LeGall, J.; Engh, R.; Schneider, M.; Hof, P.; Huber, R. Crystal structure of the xanthine oxidase-related aldehyde oxido-reductase from D. gigas. *Science* **1995**, *270*, 1170−1176.
(15) Xia, M.; Dempski, R.; Hille, R. The reductive half-reaction of xanthine oxidase: reaction with aldehyde substrates and identification of the catalytically labile oxygen. *J. Biol. Chem.* **1999**, *274*, 3323−3330.
(16) Kisker, C.; Schindelin, H.; Rees, D. C. Molybdenum-cofactor-containing enzymes: structure and mechanism. *Annu. Rev. Biochem.* **1997**, *66*, 233−267.
(17) Manikandan, P.; Choi, E.-Y.; Hille, R.; Hoffman, B. M. 35 GHz ENDOR Characterization of the "Very Rapid" Signal of Xanthine Oxidase Reacted with 2-Hydroxy-6-methylpurine (13C8): Evidence against Direct Mo− C8 Interaction. *J. Am. Chem. Soc.* **2001**, *123*, 2658−2663.
(18) Nishino, T. The conversion of xanthine dehydrogenase to xanthine oxidase and the role of the enzyme in reperfusion injury. *J. Biochem.* **1994**, *116*, 1−6.
(19) Kelley, E. E.; Khoo, N. K.; Hundley, N. J.; Malik, U. Z.; Freeman, B. A.; Tarpey, M. M. Hydrogen peroxide is the major oxidant product of xanthine oxidase. *Free Radic. Biol. Med.* **2010**, *48*, 493−498.
(20) Flemmig, J.; Kuchta, K.; Arnhold, J.; Rauwald, H. Olea europaea leaf (Ph. Eur.) extract as well as several of its isolated phenolics inhibit the gout-related enzyme xanthine oxidase. *Phytomedicine* **2011**, *18*, 561−566.
(21) Seegmiller, J. E. The acute attack of gouty arthritis. *Arthritis Rheum.* **1965**, *8*, 714−725.
(22) Nieto, F. J.; Iribarren, C.; Gross, M. D.; Comstock, G. W.; Cutler, R. G. Uric acid and serum antioxidant capacity: a reaction to atherosclerosis? *Atherosclerosis* **2000**, *148*, 131−139.
(23) Kanellis, J.; Kang, D.-H. Uric Acid as A Mediator of Endothelial Dysfunction, Inflammation, and Vascular Disease. In *Seminars in Nephrology*, Elsevier, 2005; *25*, pp 39−42.
(24) Choi, H. K.; Mount, D. B.; Reginato, A. M. Pathogenesis of gout. *Ann. Intern. Med.* **2005**, *143*, 499−516.
(25) Burke, A.; Smyth, E.; FitzGerald, G. A. Analgesic-antipyretic Agents; Pharmacotherapy of Gout. In *Pharmacological Basis of Therapeutics*, 5th ed.; 2006; Vol. *1*, p 706.
(26) Choi, H. K.; Ford, E. S.; Li, C.; Curhan, G. Prevalence of the metabolic syndrome in patients with gout: the Third National Health and Nutrition Examination Survey. *Arthritis Rheum.* **2007**, *57*, 109−115.
(27) Obermayr, R. P.; Temml, C.; Gutjahr, G.; Knechtelsdorfer, M.; Oberbauer, R.; Klauser-Braun, R. Elevated uric acid increases the risk for kidney disease. *J. Am. Soc. Nephrol.* **2008**, *19*, 2407−2413.
(28) Khanna, D.; Fitzgerald, J. D.; Khanna, P. P.; Bae, S.; Singh, M. K.; Neogi, T.; Pillinger, M. H.; Merill, J.; Lee, S.; Prakash, S.; et al. 2012 American College of Rheumatology guidelines for management of gout. Part 1: systematic nonpharmacologic and pharmacologic therapeutic approaches to hyperuricemia. *Arthritis Care Res.* **2012**, *64*, 1431−1446.
(29) Khanna, D.; Khanna, P. P.; Fitzgerald, J. D.; Singh, M. K.; Bae, S.; Neogi, T.; Pillinger, M. H.; Merill, J.; Lee, S.; Prakash, S.; et al. 2012 American College of Rheumatology guidelines for management of gout. Part 2: therapy and antiinflammatory prophylaxis of acute gouty arthritis. *Arthritis Care Res.* **2012**, *64*, 1447−1461.
(30) Nguyen, M. T. T.; Awale, S.; Tezuka, Y.; Le Tran, Q.; Kadota, S. Xanthine oxidase inhibitors from the heartwood of Vietnamese Caesalpinia sappan. *Chem. Pharm. Bull.* **2005**, *53*, 984−988.
(31) Higgins, P.; Ferguson, L. D.; Walters, M. R. Xanthine oxidase inhibition for the treatment of stroke disease: a novel therapeutic approach. *Expert Rev. Cardiovasc. Ther.* **2011**, *9*, 399−401.
(32) Elion, G. B.; Callahan, S.; Nathan, H.; Bieber, S.; Rundles, R. W.; Hitchings, G. H. Potentiation by inhibition of drug degradation: 6-substituted purines and xanthine oxidase. *Biochem. Pharmacol.* **1963**, *12*, 85−93.
(33) Elion, G. B. Enzymatic and metabolic studies with allopurinol. *Ann. Rheum. Dis.* **1966**, *25*, 608.
(34) Massey, V.; Komai, H.; Palmer, G.; Elion, G. B. On the mechanism of inactivation of xanthine oxidase by allopurinol and other pyrazolo [3, 4-d] pyrimidines. *J. Biol. Chem.* **1970**, *245*, 2837−2844.
(35) Singer, J. Z.; Wallace, S. L. The allopurinol hypersensitivity syndrome. Unnecessary morbidity and mortality. *Arthritis Rheum.* **1986**, *29*, 82−87.
(36) Rødevand, E.; Sletvold, O.; Kvande, K. T. Side effects off allopurinol. *Tidsskr. Nor. Legeforen.* **2004**, *124*, 2618−2619.
(37) Halevy, S.; Ghislain, P.-D.; Mockenhaupt, M.; Fagot, J.-P.; Bavinck, J. N. B.; Sidoroff, A.; Naldi, L.; Dunant, A.; Viboud, C.; Roujeau, J.-C. Allopurinol is the most common cause of Stevens-Johnson syndrome and toxic epidermal necrolysis in Europe and Israel. *J. Am. Acad. Dermatol.* **2008**, *58*, 25−32.
(38) Baker, B.; Hendrickson, J. Irreversible enzyme inhibitors XCII. Inhibition of xanthine oxidase by some purines and pyr midines. *J. Pharm. Sci.* **1967**, *56*, 955−959.
(39) Hille, R.; Massey, V. Tight binding inhibitors of xanthine oxidase. *Pharmacol. Ther.* **1981**, *14*, 249−263.
(40) Hawkes, T. R.; George, G. N.; Bray, R. The structure of the inhibitory complex of alloxanthine (1 H-pyrazolo [3, 4-d] pyrimidine-4, 6-diol) with the molybdenum centre of xanthine oxidase from electron-paramagnetic-resonance spectroscopy. *Biochem. J.* **1984**, *218*, 961−968.
(41) Skibo, E. B. Noncompetitive and irreversible inhibition of xanthine oxidase by benzimidazole analogs acting at the functional flavin adenine dinucleotide cofactor. *Biochemistry* **1986**, *25*, 4189−4194.
(42) Sato, S.; Tatsumi, K.; Nishino, T. A Novel Xanthine Dehydrogenase Inhibitor (BOF-4272). In *Purine and Pyrimidine Metabolism in Man VII*, Springer, 1991; pp 135−138.
(43) Nagamatsu, T.; Yamasaki, H.; Fujita, T.; Endo, K.; Machida, H. Novel xanthine oxidase inhibitor studies. Part 2. Synthesis and xanthine oxidase inhibitory activities of 2-substituted 6-alkylidenehy-

drazino-or 6-arylmethylidenehydrazino-7H-purines and 3-and/or 5-substituted 9H-1, 2, 4-triazolo [3, 4-i] purines. *J. Chem. Soc., Perkin Trans. 1* **1999**, 3117−3125.

(44) Truglio, J. J.; Theis, K.; Leimkühler, S.; Rappa, R.; Rajagopalan, K.; Kisker, C. Crystal structures of the active and alloxanthine-inhibited forms of xanthine dehydrogenase from Rhodobacter capsulatus. *Structure* **2002**, *10*, 115−125.

(45) Okamoto, K.; Eger, B. T.; Nishino, T.; Kondo, S.; Pai, E. F.; Nishino, T. An extremely potent inhibitor of xanthine oxidoreductase: crystal structure of the enzyme-inhibitor complex and mechanism of inhibition. *J. Biol. Chem.* **2003**, *278*, 1848−1855.

(46) Okamoto, K.; Matsumoto, K.; Hille, R.; Eger, B. T.; Pai, E. F.; Nishino, T. The crystal structure of xanthine oxidoreductase during catalysis: implications for reaction mechanism and enzyme inhibition. *Proc. Natl. Acad. Sci. U.S.A.* **2004**, *101*, 7931−7936.

(47) Matsumoto, K.; Okamoto, K.; Ashizawa, N.; Nishino, T. FYX-051: a novel and potent hybrid-type inhibitor of xanthine oxidoreductase. *J. Pharmacol. Exp. Ther.* **2011**, *336*, 95−103.

(48) Fukunari, A.; Okamoto, K.; Nishino, T.; Eger, B. T.; Pai, E. F.; Kamezawa, M.; Yamada, I.; Kato, N. Y-700 [1-[3-Cyano-4-(2, 2-dimethylpropoxy) phenyl]-1H-pyrazole-4-carboxylic acid]: a potent xanthine oxidoreductase inhibitor with hepatic excretion. *J. Pharmacol. Exp. Ther.* **2004**, *311*, 519−528.

(49) Tamta, H.; Thilagavathi, R.; Chakraborti, A. K.; Mukhopadhyay, A. K. 6-(N-benzoylamino) purine as a novel and potent inhibitor of xanthine oxidase: inhibition mechanism and molecular modeling studies. *J. Enzyme Inhib. Med. Chem.* **2005**, *20*, 317−324.

(50) Pacher, P.; Nivorozhkin, A.; Szabó, C. Therapeutic effects of xanthine oxidase inhibitors: renaissance half a century after the discovery of allopurinol. *Pharmacol. Rev.* **2006**, *58*, 87−114.

(51) Wortmann, R.; Ridolfo, A.; Lightfoot, R., Jr; Fox, I. Antihyperuricemic properties of amflutizole in gout. *J. Rheumatol.* **1985**, *12*, 540−543.

(52) Baldwin, J. J.; Kasinger, P.; Novello, F.; Sprague, J.; Duggan, D. 4-Trifluoromethylimidazoles and 5-(4-pyridyl)-1, 2, 4-triazoles, new classes of xanthine oxidase inhibitors. *J. Med. Chem.* **1975**, *18*, 895−900.

(53) Springer, R. H.; Dimmitt, M. K.; Novinson, T.; O'Brien, D. E.; Robins, R. K.; Simon, L. N.; Miller, J. P. Synthesis and enzymic activity of some novel xanthine oxidase inhibitors. 3-substituted 5, 7-dihydroxypyrazolo [1, 5-a] pyrimidines. *J. Med. Chem.* **1976**, *19*, 291−296.

(54) Silipo, C.; Hansch, C. Correlation analysis of Baker's studies on enzyme inhibition. 1. Guanine deaminase, xanthine oxidase, dihydrofolate reductase, and complement. *J. Med. Chem.* **1976**, *19*, 62−71.

(55) Okamoto, K.; Nishino, T. Mechanism of Inhibition of Xanthine Oxidase with a New Tight Binding Inhibitor (*). *J. Biol. Chem.* **1995**, *270*, 7816−7821.

(56) Komoriya, K.; Osada, Y.; Hasegawa, M.; Horiuchi, H.; Kondo, S.; Couch, R. C.; Griffin, T. B. Hypouricemic effect of allopurinol and the novel xanthine oxidase inhibitor TEI-6720 in chimpanzees. *Eur. J. Pharmacol.* **1993**, *250*, 455−460.

(57) Osada, Y.; Tsuchimoto, M.; Fukushima, H.; Takahashi, K.; Kondo, S.; Hasegawa, M.; Komoriya, K. Hypouricemic effect of the novel xanthine oxidase inhibitor, TEI-6720, in rodents. *Eur. J. Pharmacol.* **1993**, *241*, 183−188.

(58) Becker, M. A.; Schumacher, H. R., Jr; Wortmann, R. L.; MacDonald, P. A.; Eustace, D.; Palo, W. A.; Streit, J.; Joseph-Ridge, N. Febuxostat compared with allopurinol in patients with hyperuricemia and gout. *N. Engl. J. Med.* **2005**, *353*, 2450−2461.

(59) Yamada, I.; Fukunari, A.; Osajima, T.; Kamezawa, M.; Mori, H.; Iwane, J. Pharmacokinetics/pharmacodynamics of Y-700, a novel xanthine oxidase inhibitor, in rats and man. *Nucleosides, Nucleotides Nucleic Acids* **2004**, *23*, 1123−1125.

(60) Hashimoto, T.; Fukunari, A.; Yamada, I.; Yanaka, N.; Chen, D.; Kato, N. Y-700, a novel inhibitor of xanthine oxidase, suppresses the development of colon aberrant crypt foci and cell proliferation in 1, 2-dimethylhydrazine-treated mice. *Biosci. Biotechnol. Biochem.* **2005**, *69*, 209−211.

(61) Uematsu, T.; Nakashima, M. Pharmacokinetic and pharmacodynamic properties of a novel xanthine oxidase inhibitor, BOF-4272, in healthy volunteers. *J. Pharmacol. Exp. Ther.* **1994**, *270*, 453−459.

(62) Shimo, T.; Ashizawa, N.; Moto, M.; Matsumoto, K.; Iwanaga, T.; Nagata, O. FYX-051, a xanthine oxidoreductase inhibitor, induces nephropathy in rats, but not in monkeys. *Toxicol. Pathol.* **2009**, *37*, 438−445.

(63) Hosoya, T.; Ishikawa, T.; Ogawa, Y.; Sakamoto, R.; Ohashi, T. Multicenter, open-label study of long-term topiroxostat (FYX-051) administration in Japanese hyperuricemic patients with or without gout. *Clin. Drug Investig.* **2018**, *38*, 1135−1143.

(64) Sato, T.; Ashizawa, N.; Matsumoto, K.; Iwanaga, T.; Nakamura, H.; Inoue, T.; Nagata, O. Discovery of 3-(3-cyano-4-pyridyl)-5-(4-pyridyl)-1, 2, 4-triazole, FYX-051-a xanthine oxidoreductase inhibitor for the treatment of hyperuricemia. *Bioorg. Med. Chem. Lett.* **2009**, *19*, 6225−6229.

(65) Chen, C.; Lü, J.-M.; Yao, Q. Hyperuricemia-related diseases and xanthine oxidoreductase (XOR) inhibitors: an overview. *Med. Sci. Monit.* **2016**, *22*, 2501.

(66) Nakamura, T.; Murase, T.; Nampei, M.; Morimoto, N.; Ashizawa, N.; Iwanaga, T.; Sakamoto, R. Effects of topiroxostat and febuxostat on urinary albumin excretion and plasma xanthine oxidoreductase activity in db/db mice. *Eur. J. Pharmacol.* **2016**, *780*, 224−231.

(67) Ojha, R.; Singh, J.; Ojha, A.; Singh, H.; Sharma, S.; Nepali, K. An updated patent review: xanthine oxidase inhibitors for the treatment of hyperuricemia and gout (2011-2015). *Expert Opin. Ther. Pat.* **2017**, *27*, 311−345.

(68) Huneycutt, E.; Board, C.; Clements, J. N. Lesinurad, a selective URAT-1 inhibitor with a novel mechanism in combination with a xanthine oxidase inhibitor, for hyperuricemia associated with gout. *J. Pharm. Pract.* **2018**, *31*, 670−677.

(69) Masuoka, N.; Kubo, I. Characterization of the xanthine oxidase inhibitory activity of alk (en) yl phenols and related compounds. *Phytochemistry* **2018**, *155*, 100−106.

(70) Mehmood, A.; Ishaq, M.; Zhao, L.; Safdar, B.; Rehman, Au.; Munir, M.; Raza, A.; Nadeem, M.; Iqbal, W.; Wang, C. Natural compounds with xanthine oxidase inhibitory activity: A review. *Chem. Biol. Drug Des.* **2019**, *93*, 387−418.

(71) Malik, N.; Dhiman, P.; Khatkar, A. In silico and 3D QSAR studies of natural based derivatives as xanthine oxidase inhibitors. *Curr. Top. Med. Chem.* **2019**, *19*, 123−138.

(72) Luna, G.; Dolzhenko, A. V.; Mancera, R. L. Inhibitors of Xanthine Oxidase: Scaffold Diversity and Structure-Based Drug Design. *ChemMedChem* **2019**, *14*, 714−743.

(73) Gunduğdu, Ö.; Noma, S. A. A.; Taskin-Tok, T.; Ateş, B.; Kishali, N. Evaluation of xanthine oxidase inhibitor properties on isoindoline-1, 3-dion derivatives and calculation of interaction mechanism. *J. Mol. Struct.* **2020**, *1204*, No. 127523.

(74) Kumar, R.; Joshi, G.; Kler, H.; Kalra, S.; Kaur, M.; Arya, R. Toward an understanding of structural insights of xanthine and aldehyde oxidases: an overview of their inhibitors and role in various diseases. *Med. Res. Rev.* **2018**, *38*, 1073−1125.

(75) Chen, L. X.; Schumacher, H. R. Gout: an evidence-based review. *J. Clin. Rheumatol.* **2008**, *14*, S55−S62.

(76) Richette, P.; Bardin, T. Gout. *The Lancet* **2010**, *375*, 318−328.

(77) Vos, T.; Barber, R. M.; Bell, B.; Bertozzi-Villa, A.; Biryukov, S.; Bolliger, I.; Charlson, F.; Davis, A.; Degenhardt, L.; Dicker, D.; et al. Global, regional, and national incidence, prevalence, and years lived with disability for 301 acute and chronic diseases and injuries in 188 countries, 1990−2013: a systematic analysis for the Global Burden of Disease Study 2013. *Lancet* **2015**, *386*, 743−800.

(78) Metz, S.; Thiel, W. A combined QM/MM study on the reductive half-reaction of xanthine oxidase: substrate orientation and mechanism. *J. Am. Chem. Soc.* **2009**, *131*, 14885−14902.

(79) Kela, U.; Vijayvargiya, R. Studies on the mechanism of action of 6-mercaptopurine. Interaction with copper and xanthine oxidase. *Biochem. J.* **1981**, *193*, 799−803.

(80) Okamoto, K.; Eger, B. T.; Nishino, T.; Pai, E. F.; Nishino, T. Mechanism of inhibition of xanthine oxidoreductase by allopurinol: crystal structure of reduced bovine milk xanthine oxidoreductase bound with oxipurinol. *Nucleosides, Nucleotides Nucleic Acids* **2008**, *27*, 888−893.

(81) Elion, G. B.; Kovensky, A.; Hitchings, G. H.; Metz, E.; Rundles, R. W. Metabolic studies of allopurinol, an inhibitor of xanthine oxidase. *Biochem. Pharmacol.* **1966**, *15*, 863−880.

(82) Spector, T.; Johns, D. 4-Hydroxypyrazolo (3, 4-d) pyrimidine as a substrate for xanthine oxidase: loss of conventional substrate activity with catalytic cycling of the enzyme. *Biochem. Biophys. Res. Commun.* **1970**, *38*, 583−589.

(83) Edmondson, D.; Ballou, D.; Van Heuvelen, A.; Palmer, G.; Massey, V. Kinetic studies on the substrate reduction of xanthine oxidase. *J. Biol. Chem.* **1973**, *248*, 6135−6144.

(84) Olson, J. S.; Ballou, D. P.; Palmer, G.; Massey, V. The mechanism of action of xanthine oxidase. *J. Biol. Chem.* **1974**, *249*, 4363−4382.

(85) Spector, T.; Hall, W. W.; Krenitsky, T. A. Human and bovine xanthine oxidases: inhibition studies with oxipurinol. *Biochem. Pharmacol.* **1986**, *35*, 3109−3114.

(86) Mondal, M. S.; Mitra, S. Kinetics and thermodynamics of the molecular mechanism of the reductive half-reaction of xanthine oxidase. *Biochemistry* **1994**, *33*, 10305−10312.

(87) Stockert, A. L.; Shinde, S. S.; Anderson, R. F.; Hille, R. The reaction mechanism of xanthine oxidase: evidence for two-electron chemistry rather than sequential one-electron steps. *J. Am. Chem. Soc.* **2002**, *124*, 14554−14555.

(88) Choi, E.-Y.; Stockert, A. L.; Leimkühler, S.; Hille, R. Studies on the mechanism of action of xanthine oxidase. *J. Inorg. Biochem.* **2004**, *98*, 841−848.

(89) Yamaguchi, Y.; Matsumura, T.; Ichida, K.; Okamoto, K.; Nishino, T. Human xanthine oxidase changes its substrate specificity to aldehyde oxidase type upon mutation of amino acid residues in the active site: roles of active site residues in binding and activation of purine substrate. *J. Biochem.* **2007**, *141*, 513−524.

(90) Amano, T.; Ochi, N.; Sato, H.; Sakaki, S. Oxidation reaction by Xanthine oxidase. Theoretical study of reaction mechanism. *J. Am. Chem. Soc.* **2007**, *129*, 8131−8138.

(91) Alfaro, J. F.; Jones, J. P. Studies on the mechanism of aldehyde oxidase and xanthine oxidase. *J. Org. Chem.* **2008**, *73*, 9469−9472.

(92) Bayse, C. A. Density-functional theory models of xanthine oxidoreductase activity: comparison of substrate tautomerization and protonation. *Dalton Trans.* **2009**, 2306−2314.

(93) Metz, S.; Thiel, W. QM/MM studies of xanthine oxidase: variations of cofactor, substrate, and active-site Glu802. *J. Phys. Chem. B* **2010**, *114*, 1506−1517.

(94) Du, Y.; Liu, Z.; Qiao, F.; Wang, S.; Chen, K.; Zhang, X. Computational exploration of reactive fragment for mechanism-based inhibition of xanthine oxidase. *J. Organomet. Chem.* **2018**, *864*, 58−67.

(95) Ribeiro, P. M. G.; Fernandes, H. S.; Maia, L. B.; Sousa, S. F.; Moura, J. J.; Cerqueira, N. M. The complete catalytic mechanism of xanthine oxidase: a computational study. *Inorg. Chem. Front.* **2021**, *8*, 405−416.

(96) Bray, M. R.; Deeth, R. J. The catalytic activity of xanthine oxidase: mechanistic insights throughcomputer modelling. *J. Chem. Soc., Dalton Trans.* **1997**, 1267−1268.

(97) Zhang, X.-H.; Wu, Y.-D. A theoretical study on the mechanism of the reductive half-reaction of xanthine oxidase. *Inorg. Chem.* **2005**, *44*, 1466−1471.

(98) Ilich, P.; Hille, R. Mechanism of Formamide Hydroxylation Catalyzed by a Molybdenum− Dithiolene Complex: A Model for Xanthine Oxidase Reactivity. *J. Phys. Chem. B* **1999**, *103*, 5406−5412.

(99) Altschul, S. F.; Wootton, J. C.; Gertz, E. M.; Agarwala, R.; Morgulis, A.; Schäffer, A. A.; Yu, Y. K. Protein database searches using compositionally adjusted substitution matrices. *FEBS J.* **2005**, *272*, 5101−5109.

(100) Altschul, S. F.; Madden, T. L.; Schäffer, A. A.; Zhang, J.; Zhang, Z.; Miller, W.; Lipman, D. J. Gapped BLAST and PSI-BLAST: a new generation of protein database search programs. *Nucleic Acids Res.* **1997**, *25*, 3389−3402.

(101) Pearson, A.; Godber, B.; Eisenthal, R.; Taylor, G.; Harrison, R. Human milk xanthine dehydrogenase is incompletely converted to the oxidase form in the absence of proteolysis *A Structural Explanation*, 2006.

(102) Eswar, N.; Eramian, D.; Webb, B.; Shen, M.-Y.; Sali, A. Protein Structure Modeling with MODELLER. In *Structural proteomics*, Springer, 2008; pp 145−159.

(103) Eswar, N.; Webb, B.; Marti-Renom, M. A.; Madhusudhan, M.; Eramian, D.; Shen, My.; Pieper, U.; Sali, A. Comparative protein structure modeling using Modeller. *Curr. Protoc. Bioinf.* **2006**, *15*, 5.6.1−5.6.30.

(104) Moult, J.; Fidelis, K.; Kryshtafovych, A.; Schwede, T.; Tramontano, A. Critical assessment of methods of protein structure prediction (CASP)—round x. *Proteins* **2014**, *82*, 1−6.

(105) Haas, J.; Roth, S.; Arnold, K.; Kiefer, F.; Schmidt, T.; Bordoli, L.; Schwede, T. The Protein Model Portal—a comprehensive resource for protein structure and model information. *Database* **2013**, *2013*, bat031.

(106) Ferreira, P.; Cerqueira, N. M.; Brás, N. F.; Fernandes, P. A.; Ramos, M. J. Parametrization of Molybdenum Cofactors for the AMBER Force Field. *J. Chem. Theory Comput.* **2018**, *14*, 2538−2548.

(107) Li, P.; Merz, K. M., Jr. MCPB.py: A Python Based Metal Center Parameter Builder. *J. Chem. Inf. Model.* **2016**, *56*, 599−604.

(108) Carvalho, A. T. P.; Teixeira, A. F.; Ramos, M. J. Parameters for molecular dynamics simulations of iron-sulfur proteins. *J. Comput. Chem.* **2013**, *34*, 1540−1548.

(109) Bayly, C. I.; Cieplak, P.; Cornell, W.; Kollman, P. A. A well-behaved electrostatic potential based method using charge restraints for deriving atomic charges: the RESP model. *J. Phys. Chem. A* **1993**, *97*, 10269−10280.

(110) Dupradeau, F.-Y.; Pigache, A.; Zaffran, T.; Savineau, C.; Lelong, R.; Grivel, N.; Lelong, D.; Rosanski, W.; Cieplak, P. The REd. Tools: Advances in RESP and ESP charge derivation and force field library building. *Phys. Chem. Chem. Phys.* **2010**, *12*, 7821−7839.

(111) Vanquelef, E.; Simon, S.; Marquant, G.; Garcia, E.; Klimerak, G.; Delepine, J. C.; Cieplak, P.; Dupradeau, F.-Y. RED Server: a web service for deriving RESP and ESP charges and building force field libraries for new molecules and molecular fragments. *Nucleic Acids Res.* **2011**, *39*, W511−W517.

(112) Wang, J.; Wolf, R. M.; Caldwell, J. W.; Kollman, P. A.; Case, D. A. Development and testing of a general amber force field. *J. Comput. Chem.* **2004**, *25*, 1157−1174.

(113) Wang, J.; Wang, W.; Kollman, P. A.; Case, D. A. Automatic atom type and bond type perception in molecular mechanical calculations. *J. Mol. Graph. Model.* **2006**, *25*, 247−260.

(114) Olsson, M. H. M.; Søndergaard, C. R.; Rostkowski, M.; Jensen, J. H. PROPKA3: consistent treatment of internal and surface residues in empirical p K a predictions. *J. Chem. Theory Comput.* **2011**, *7*, 525−537.

(115) Søndergaard, C. R.; Olsson, M. H.; Rostkowski, M.; Jensen, J. H. Improved treatment of ligands and coupling effects in empirical calculation and rationalization of p K a values. *J. Chem. Theory Comput.* **2011**, *7*, 2284−2295.

(116) Pauff, J. M.; Hemann, C. F.; Jünemann, N.; Leimkühler, S.; Hille, R. The role of arginine 310 in catalysis and substrate specificity in xanthine dehydrogenase from Rhodobacter capsulatus. *J. Biol. Chem.* **2007**, *282*, 12785−12790.

(117) Pauff, J. M.; Zhang, J.; Bell, C. E.; Hille, R. Substrate orientation in xanthine oxidase: crystal structure of enzyme in reaction with 2-hydroxy-6-methylpurine. *J. Biol. Chem.* **2008**, *283*, 4818−4824.

(118) Metz, S.; Wang, D.; Thiel, W. Reductive half-reaction of aldehyde oxidoreductase toward acetaldehyde: a combined QM/MM study. *J. Am. Chem. Soc.* **2009**, *131*, 4628−4640.

(119) Okamoto, K.; Kusano, T.; Nishino, T. Chemical nature and reaction mechanisms of the molybdenum cofactor of xanthine oxidoreductase. *Curr. Pharm. Des.* **2013**, *19*, 2606−2614.

(120) Schafmeister, C.; Ross, W.; Romanovski, V.. *LEaP*.University of California: San Francisco, 1995.

(121) DA, C.; Ben-Shalom, S.; Brozell, D.; Cerutti, T., III; Cheatham, V., III; Cruzeiro, T.; Darden, R.; Duke, D. G.; Gilson, M.; Gohlke, H.. *AMBER 18*; University of California: San Francisco, 2018.

(122) Jorgensen, W. L.; Chandrasekhar, J.; Madura, J. D.; Impey, R. W.; Klein, M. L. Comparison of simple potential functions for simulating liquid water. *J. Chem. Phys.* **1983**, *79*, 926−935.

(123) Maier, J. A.; Martinez, C.; Kasavajhala, K.; Wickstrom, L.; Hauser, K. E.; Simmerling, C. ff14SB: improving the accuracy of protein side chain and backbone parameters from ff99SB. *J. Chem. Theory Comput.* **2015**, *11*, 3696−3713.

(124) Zwanzig, R. Nonlinear generalized Langevin equations. *J. Stat. Phys.* **1973**, *9*, 215−220.

(125) Loncharich, R. J.; Brooks, B. R.; Pastor, R. W. Langevin dynamics of peptides: The frictional dependence of isomerization rates of N-acetylalanyl-N′-methylamide. *Biopolymers* **1992**, *32*, 523−535.

(126) Gillespie, D. T. The chemical Langevin equation. *J. Chem. Phys.* **2000**, *113*, 297−306.

(127) Ryckaert, J.-P.; Ciccotti, G.; Berendsen, H. J. Numerical integration of the cartesian equations of motion of a system with constraints: molecular dynamics of n-alkanes. *J. Comput. Phys.* **1977**, *23*, 327−341.

(128) Essmann, U.; Perera, L.; Berkowitz, M. L.; Darden, T.; Lee, H.; Pedersen, L. G. A smooth particle mesh Ewald method. *J. Chem. Phys.* **1995**, *103*, 8577−8593.

(129) Salomon-Ferrer, R.; Gotz, A. W.; Poole, D.; Le Grand, S.; Walker, R. C. Routine microsecond molecular dynamics simulations with AMBER on GPUs. 2. Explicit solvent particle mesh Ewald. *J. Chem. Theory Comput.* **2013**, *9*, 3878−3888.

(130) Roe, D. R.; Cheatham, T. E., III PTRAJ and CPPTRAJ: software for processing and analysis of molecular dynamics trajectory data. *J. Chem. Theory Comput.* **2013**, *9*, 3084−3095.

(131) Bakan, A.; Meireles, L. M.; Bahar, I. ProDy: protein dynamics inferred from theory and experiments. *Bioinformatics* **2011**, *27*, 1575−1577.

(132) Oliphant, T. E. *A guide to NumPy*, 2nd ed.; Trelgol Publishing: USA, 2015; Vol. *1*.

(133) Van Der Walt, S.; Colbert, S. C.; Varoquaux, G. The NumPy array: a structure for efficient numerical computation. *Comput. Sci. Eng.* **2011**, *13*, 22−30.

(134) Hunter, J. D. Matplotlib: A 2D graphics environment. *Comput. Sci. Eng.* **2007**, *9*, 90−95.

(135) McKinney, W. In Data Structures for Statistical Computing in Python, Proceedings of the 9th Python in Science Conference, Austin, TX, 2010, Vol. 445, p. 51−56.

(136) Seabold, S.; Perktold, J. Statsmodels: Econometric and Statistical Modeling with Python, Proceedings of the 9th Python in Science Conference, Austin, TX, 2010; Vol. 57; p. 61.

(137) Williams, T.; Kelley, C.. *Gnuplot 5.2: An Interactive Plotting Program*, http://www.gnuplot.Info.

(138) Likas, A.; Vlassis, N.; Verbeek, J. J. The global k-means clustering algorithm. *Pattern Recognit* **2003**, *36*, 451−461.

(139) Kollman, P. A.; Massova, I.; Reyes, C.; Kuhn, B.; Huo, S.; Chong, L.; Lee, M.; Lee, T.; Duan, Y.; Wang, W.; et al. Calculating structures and free energies of complex molecules: combining molecular mechanics and continuum models. *Acc. Chem. Res.* **2000**, *33*, 889−897.

(140) Wang, W.; Donini, O.; Reyes, C. M.; Kollman, P. A. Biomolecular simulations: recent developments in force fields, simulations of enzyme catalysis, protein-ligand, protein-protein, and protein-nucleic acid noncovalent interactions. *Annu. Rev. Biophys. Biomol. Struct.* **2001**, *30*, 211−243.

(141) Wang, J.; Hou, T.; Xu, X. Recent advances in free energy calculations with a combination of molecular mechanics and continuum models. *Curr. Comput. Aided Drug Des.* **2006**, *2*, 287−306.

(142) Homeyer, N.; Gohlke, H. Free energy calculations by the molecular mechanics Poisson− Boltzmann surface area method. *Mol. Inform.* **2012**, *31*, 114−122.

(143) Miller, B. R., III; McGee, T. D., Jr; Swails, J. M.; Homeyer, N.; Gohlke, H.; Roitberg, A. E. MMPBSA. py: an efficient program for end-state free energy calculations. *J. Chem. Theory Comput.* **2012**, *8*, 3314−3321.

(144) Hou, T.; Wang, J.; Li, Y.; Wang, W. Assessing the performance of the MM/PBSA and MM/GBSA methods. 1. The accuracy of binding free energy calculations based on molecular dynamics simulations. *J. Chem. Inf. Model.* **2011**, *51*, 69−82.

(145) Hou, T.; Wang, J.; Li, Y.; Wang, W. Assessing the performance of the molecular mechanics/Poisson Boltzmann surface area and molecular mechanics/generalized Born surface area methods. II. The accuracy of ranking poses generated from docking. *J. Comput. Chem.* **2011**, *32*, 866−877.

(146) Muzzioli, E.; Del Rio, A.; Rastelli, G. Assessing Protein Kinase Selectivity with Molecular Dynamics and MM-PBSA Binding Free Energy Calculations. *Chem. Biol. Drug Des.* **2011**, *78*, 252−259.

(147) Xu, L.; Li, Y.; Li, L.; Zhou, S.; Hou, T. Understanding microscopic binding of macrophage migration inhibitory factor with phenolic hydrazones by molecular docking, molecular dynamics simulations and free energy calculations. *Mol. Biosyst.* **2012**, *8*, 2260−2273.

(148) Genheden, S.; Kuhn, O.; Mikulskis, P.; Hoffmann, D.; Ryde, U. The normal-mode entropy in the MM/GBSA method: effect of system truncation, buffer region, and dielectric constant. *J. Chem. Inf. Model.* **2012**, *52*, 2079−2088.

(149) Sun, H.; Duan, L.; Chen, F.; Liu, H.; Wang, Z.; Pan, P.; Zhu, F.; Zhang, J. Z.; Hou, T. Assessing the performance of MM/PBSA and MM/GBSA methods. 7. Entropy effects on the performance of end-point binding free energy calculation approaches. *Phys. Chem. Chem. Phys.* **2018**, *20*, 14450−14460.

(150) Naseem-Khan, S.; Berger, M. B.; Leddin, E. M.; Maghsoud, Y.; Cisneros, G. A. Impact of Remdesivir Incorporation along the Primer Strand on SARS-CoV-2 RNA-Dependent RNA Polymerase. *J. Chem. Inf. Model.* **2022**, *62*, 2456−2465.

(151) Kratz, E. G.; Walker, A. R.; Lagardère, L.; Lipparini, F.; Piquemal, J. P.; Andrés Cisneros, G. LICHEM: A QM/MM program for simulations with multipolar and polarizable force fields. *J. Comput. Chem.* **2016**, *37*, 1019−1029.

(152) Gökcan, H.; Vázquez-Montelongo, E. A.; Cisneros, G. A. LICHEM 1.1: recent improvements and new capabilities. *J. Chem. Theory Comput.* **2019**, *15*, 3056−3065.

(153) Frisch, M. J.; Trucks, G. W.; Schlegel, H. B.; Scuseria, G. E.; Robb, M. A.; Cheeseman, J. R.; Scalmani, G.; Barone, V.; Petersson, G. A.; Nakatsuji, H.; Li, X.; Caricato, M.; Marenich, A. V.; Bloino, J.; Janesko, B. G.; Gomperts, R.; Mennucci, B.; Hratchian, H. P.; Ortiz, J. V.; Izmaylov, A. F.; Sonnenberg, J. L.; Williams; Ding, F.; Lipparini, F.; Egidi, F.; Goings, J.; Peng, B.; Petrone, A.; Henderson, T.; Ranasinghe, D.; Zakrzewski, V. G.; Gao, J.; Rega, N.; Zheng, G.; Liang, W.; Hada, M.; Ehara, M.; Toyota, K.; Fukuda, R.; Hasegawa, J.; Ishida, M.; Nakajima, T.; Honda, Y.; Kitao, O.; Nakai, H.; Vreven, T.; Throssell, K.; Montgomery, J. A., Jr.; Peralta, J. E.; Ogliaro, F.; Bearpark, M. J.; Heyd, J. J.; Brothers, E. N.; Kudin, K. N.; Staroverov, V. N.; Keith, T. A.; Kobayashi, R.; Normand, J.; Raghavachari, K.; Rendell, A. P.; Burant, J. C.; Iyengar, S. S.; Tomasi, J.; Cossi, M.; Millam, J. M.; Klene, M.; Adamo, C.; Cammi, R.; Ochterski, J. W.; Martin, R. L.; Morokuma, K.; Farkas, O.; Foresman, J. B.; Fox, D. J.. *Gaussian 16 Rev. C.01*; Wallingford, CT, 2016.

(154) Rackers, J. A.; Wang, Z.; Lu, C.; Laury, M. L.; Lagardère, L.; Schnieders, M. J.; Piquemal, J.-P.; Ren, P.; Ponder, J. W. Tinker 8: software tools for molecular design. *J. Chem. Theory Comput.* **2018**, *14*, 5273−5289.

(155) Weigend, F.; Ahlrichs, R. Balanced basis sets of split valence, triple zeta valence and quadruple zeta valence quality for H to Rn:

Design and assessment of accuracy. *Phys. Chem. Chem. Phys.* **2005**, *7*, 3297−3305.

(156) Andrae, D.; Haeussermann, U.; Dolg, M.; Stoll, H.; Preuss, H. Energy-adjustedab initio pseudopotentials for the second and third row transition elements. *Theor. Chim. Acta* **1990**, *77*, 123−141.

(157) Pritchard, B. P.; Altarawy, D.; Didier, B.; Gibson, T. D.; Windus, T. L. New basis set exchange: An open, up-to-date resource for the molecular sciences community. *J. Chem. Inf. Model.* **2019**, *59*, 4814−4820.

(158) Kratz, E. G.; Duke, R. E.; Cisneros, G. A. Long-range electrostatic corrections in multipolar/polarizable QM/MM simulations. *Theor. Chem. Acc.* **2016**, *135*, 166.

(159) Nishino, T.; Okamoto, K. Mechanistic insights into xanthine oxidoreductase from development studies of candidate drugs to treat hyperuricemia and gout. *JBIC, J. Biol. Inorg. Chem.* **2015**, *20*, 195−207.

(160) Fang, D.; Chaudret, R.; Piquemal, J.-P.; Cisneros, G. A. s. Toward a deeper understanding of enzyme reactions using the coupled ELF/NCI analysis: application to DNA repair enzymes. *J. Chem. Theory Comput.* **2013**, *9*, 2156−2160.

(161) Johnson, E. R.; Keinan, S.; Mori-Sánchez, P.; Contreras-García, J.; Cohen, A. J.; Yang, W. Revealing noncovalent interactions. *J. Am. Chem. Soc.* **2010**, *132*, 6498−6506.

(162) Lu, T.; Chen, F. Multiwfn: a multifunctional wavefunction analyzer. *J. Comput. Chem.* **2012**, *33*, 580−592.

(163) Becke, A. D.; Edgecombe, K. E. A simple measure of electron localization in atomic and molecular systems. *J. Chem. Phys.* **1990**, *92*, 5397−5403.

(164) Shuo, Y.; Xu, G.-Y.; Han, J.-P.; Bing, H.; Dou, H.; Zhang, X.-G. Nitrogen-doped porous carbon derived from dopamine-modified polypyrrole and its electrochemical capacitive behavior. *Acta Phys.-Chim. Sin.* **2015**, *31*, 685−692.

(165) Tian, L.; Chen, F.-W. Meaning and functional form of the electron localization function. *Acta Phys.-Chim. Sin.* **2011**, *27*, 2786−2792.

(166) Humphrey, W.; Dalke, A.; Schulten, K. VMD: visual molecular dynamics. *J. Mol. Graph.* **1996**, *14*, 33−38.

(167) Cui, Q.; Karplus, M. Catalysis and specificity in enzymes: a study of triosephosphate isomerase and comparison with methyl glyoxal synthase. *Protein Simulations* **2003**, *66*, 315−372.

(168) Martí, S.; Andrés, J.; Moliner, V.; Silla, E.; Tuñón, I.; Bertrán, J. Preorganization and reorganization as related factors in enzyme catalysis: the chorismate mutase case. *Chem. - Eur. J.* **2003**, *9*, 984−991.

(169) Senn, H. M.; O'Hagan, D.; Thiel, W. Insight into enzymatic C− F Bond formation from QM and QM/MM calculations. *J. Am. Chem. Soc.* **2005**, *127*, 13643−13655.

(170) Cisneros, G. A.; Perera, L.; Schaaper, R. M.; Pedersen, L. C.; London, R. E.; Pedersen, L. G.; Darden, T. A. Reaction mechanism of the ε subunit of E. coli DNA polymerase III: insights into active site metal coordination and catalytically significant residues. *J. Am. Chem. Soc.* **2009**, *131*, 1550−1556.

(171) Fang, D.; Lord, R. L.; Cisneros, G. A. Ab initio QM/MM calculations show an intersystem crossing in the hydrogen abstraction step in dealkylation catalyzed by AlkB. *J. Phys. Chem. B* **2013**, *117*, 6410−6420.

(172) Fang, D.; Cisneros, G. A. s. Alternative pathway for the reaction catalyzed by DNA dealkylase AlkB from ab initio QM/MM calculations. *J. Chem. Theory Comput.* **2014**, *10*, 5136−5148.

(173) Torabifard, H.; Cisneros, G. A. Insight into wild-type and T1372E TET2-mediated 5hmC oxidation using ab initio QM/MM calculations. *Chem. Sci.* **2018**, *9*, 8433−8445.

(174) Graham, S. E.; Syeda, F.; Cisneros, G. A. s. Computational prediction of residues involved in fidelity checking for DNA synthesis in DNA polymerase I. *Biochemistry* **2012**, *51*, 2569−2578.

(175) Dewage, S. W.; Cisneros, G. A. Computational analysis of ammonia transfer along two intramolecular tunnels in Staphylococcus aureus glutamine-dependent amidotransferase (GatCAB). *J. Phys. Chem. B* **2015**, *119*, 3669−3677.

(176) Walker, A. R.; Cisneros, G. A. s. Computational simulations of DNA polymerases: detailed insights on structure/function/mechanism from native proteins to cancer variants. *Chem. Res. Toxicol.* **2017**, *30*, 1922−1935.

(177) Swails, J.; Hernandez, C.; Mobley, D. L.; Nguyen, H.; Wang, L.-P.; Janowski, P. ParmEd, 2010, https://github.com/ParmEd/ParmEd.

(178) Team, R. C. R. A Language and Environment for Statistical Computing, https://www.r-project.org/.

(179) Leimkühler, S.; Stockert, A. L.; Igarashi, K.; Nishino, T.; Hille, R. The role of active site glutamate residues in catalysis of Rhodobacter capsulatus xanthine dehydrogenase. *J. Biol. Chem.* **2004**, *279*, 40437−40444.

(180) Cao, H.; Pauff, J. M.; Hille, R. Substrate orientation and catalytic specificity in the action of xanthine oxidase: the sequential hydroxylation of hypoxanthine to uric acid. *J. Biol. Chem.* **2010**, *285*, 28044−28053.

(181) Kim, J. H.; Ryan, M. G.; Knaut, H.; Hille, R. The reductive half-reaction of xanthine oxidase: The involvement of prototropic equilibria in the course of the catalytic sequence. *J. Biol. Chem.* **1996**, *271*, 6771−6780.

(182) Hille, R.; Hall, J.; Basu, P. The mononuclear molybdenum enzymes. *Chem. Rev.* **2014**, *114*, 3963−4038.

(183) Kirk, M. L.; Berhane, A. Correlating C−H Bond Cleavage with Molybdenum Reduction in Xanthine Oxidase. *Chem. Biodivers.* **2012**, *9*, 1756−1760.

(184) Sempombe, J.; Stein, B.; Kirk, M. L. Spectroscopic and Electronic Structure Studies Probing Covalency Contributions to C−H Bond Activation and Transition-State Stabilization in Xanthine Oxidase. *Inorg. Chem.* **2011**, *50*, 10919−10928.

(185) Kikuchi, H.; Fujisaki, H.; Furuta, T.; Okamoto, K.; Leimkühler, S.; Nishino, T. Different inhibitory potency of febuxostat towards mammalian and bacterial xanthine oxidoreductases: insight from molecular dynamics. *Sci. Rep.* **2012**, *2*, No. 331.

(186) Liu, H.; Zhang, Y.; Yang, W. How is the active site of enolase organized to catalyze two different reaction steps? *J. Am. Chem. Soc.* **2000**, *122*, 6560−6570.

(187) Pauff, J. M.; Cao, H.; Hille, R. Substrate orientation and catalysis at the Molybdenum site in xanthine oxidase. *J. Biol. Chem.* **2009**, *284*, 8760−8767.

(188) Ilich, P.; Hille, R. Tautomerization of the substrate heterocycle in the course of the reaction of xanthine oxidase. *Inorg. Chim. Acta* **1997**, *263*, 87−93.

(189) Glatigny, A.; Hof, P.; Romão, M. J.; Huber, R.; Scazzocchio, C. Altered specificity mutations define residues essential for substrate positioning in xanthine dehydrogenase. *J. Mol. Biol.* **1998**, *278*, 431−438.

(190) Kudo, M.; Moteki, T.; Sasaki, T.; Konno, Y.; Ujiie, S.; Onose, A.; Mizugaki, M.; Ishikawa, M.; Hiratsuka, M. Functional characterization of human xanthine oxidase allelic variants. *Pharmacogenet. Genomics* **2008**, *18*, 243−251.

(191) Sakamoto, N.; Yamamoto, T.; Moriwaki, Y.; Teranishi, T.; Toyoda, M.; Onishi, Y.; Kuroda, S.; Sakaguchi, K.; Fujisawa, T.; Maeda, M.; Hada, T. Identification of a new point mutation in the human xanthine dehydrogenase gene responsible for a case of classical type I xanthinuria. *Hum. Genet.* **2001**, *108*, 279−283.

(192) Ichida, K.; Amaya, Y.; Kamatani, N.; Nishino, T.; Hosoya, T.; Sakai, O. Identification of two mutations in human xanthine dehydrogenase gene responsible for classical type I xanthinuria. *J. Clin. Invest.* **1997**, *99*, 2391−2397.

(193) Gok, F.; Ichida, K.; Topaloglu, R. Mutational analysis of the xanthine dehydrogenase gene in a Turkish family with autosomal recessive classical xanthinuria. *Nephrol., Dial., Transplant.* **2003**, *18*, 2278−2283.

(194) Stiburkova, B.; Krijt, J.; Vyletal, P.; Bartl, J.; Gerhatova, E.; Korinek, M.; Sebesta, I. Novel mutations in xanthine dehydrogenase/oxidase cause severe hypouricemia: biochemical and molecular genetic analysis in two Czech families with xanthinuria type I. *Clin. Chim. Acta* **2012**, *413*, 93−99.

(195) Arikyants, N.; Sarkissian, A.; Hesse, A.; Eggermann, T.; Leumann, E.; Steinmann, B. Xanthinuria type I: a rare cause of urolithiasis. *Pediatr. Nephrol.* **2007**, *22*, 310−314.

(196) Xu, T.; Xie, X.; Zhang, Z.; Zhao, N.; Deng, Y.; Li, P. A novel mutation in xanthine dehydrogenase in a case with xanthinuria in Hunan province of China. *Clin. Chim. Acta* **2020**, *504*, 168−171.

(197) Tanaka, K.-i.; Kanazawa, I.; Yamasaki, H.; Hasegawa, H.; Ichida, K.; Sugimoto, T. Xanthinuria type I with a novel mutation of xanthine dehydrogenase. *Am. J. Med. Sci.* **2015**, *350*, 155−156.

https://doi.org/10.1021/acscatal.3c01245
ACS Catal. 2023, 13, 6023−6043